Chapter 3
Grind-Hardening Process Modelling

Abstract Grind-hardening process is a complex hybrid process integrating heat treatment process with high material rate grinding. The modelling of the process thus is quite complex and a number of aspects need to be considered. The present chapter presents a holistic model able to predict the grinding forces, temperature distribution, metallurgical changes, surface hardness and residual stresses. The model is composed of a number of sub-models that are also verified experimentally.

3.1 Introduction

The grinding process is characterized by a series of stochastic engagement between the grinding wheel grits and the workpiece, that depend on a number of factors such as the grinding wheel microstructure, the process parameters and the geometry of the grinding wheel. These engagements result in the generation of the chips but also in heat within the grinding area. The modelling of the grinding process (and grind-hardening process as the mechanics and kinematics of the process are the same), requires the consideration of the topography of the grinding wheel. Topography models can be developed and feed info in chip formation models in order to derive estimations of the grinding exerted forces and the heat generated. It has been shown, mainly for the grinding process, that strong relationships exist between the topography of the grinding wheel, the process forces, the heat generation and the grinding wheel wear.

Based on the wheel topography models, the chip thickness and the surface roughness can be predicted. As already mentioned, besides the forces and the generated energy, the topography of the grinding wheel affects the grinding area temperature and the subsequent metallurgical transformations and the sub-surface integrity of the ground part. In the present chapter, an approach to modelling the various aspects of the grind-hardening process is presented. As it is expected, the model is composed of a number of sub-models, as can be seen in Fig. 3.1, that

K. Salonitis, *Grind Hardening Process*, SpringerBriefs in Manufacturing and Surface Engineering, DOI 10.1007/978-3-319-19372-4_3

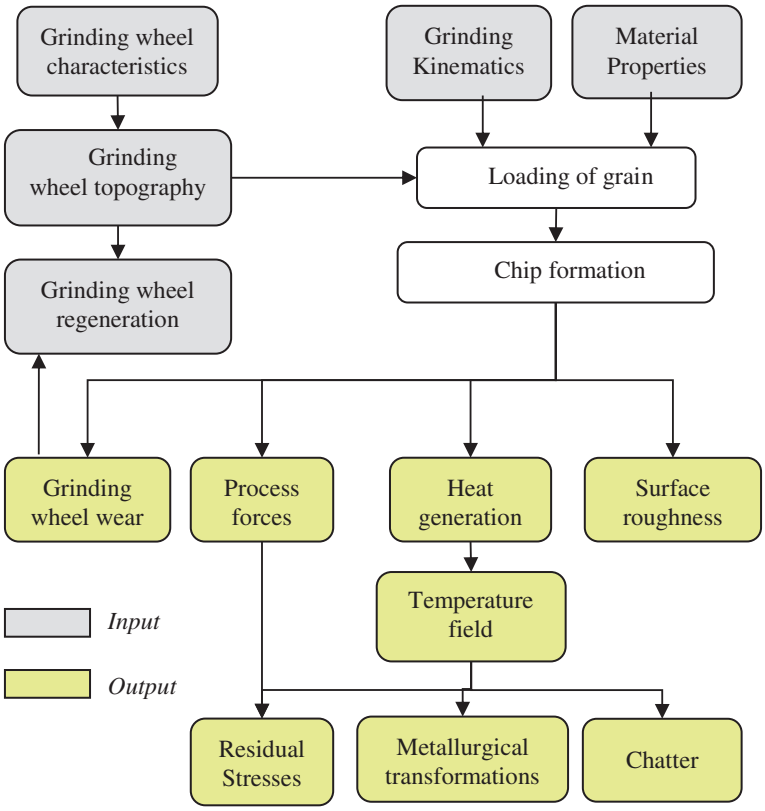

Fig. 3.1 Modelling grinding processes

are either solved analytically or with the use of finite element method. All the sub-models presented are validated with experimental results and provide insights on how the process behaves under different processing conditions.

3.2 Grinding Kinematics—Grinding Wheel Topography

Toenshoff et al. [1] indicated that the grinding process kinematics is a series of stochastic engagements that depend on a number of factors such as the microstructure of the grinding wheel, the process parameters and the geometric parameters. Through the analysis of grinding kinematics, a number of process characteristics can be determined that will be used later on for estimating the grinding forces and the process energy.

The grinding wheel topography modelling is very important in understanding the result of the interaction between the grinding wheel and the workpiece material.

The microstructure of the grinding wheel is characterized by the number of static and active grains. Active grains are considered to be the ones that are in contact with the workpiece material and contribute to the formulation of chips and the heat generation due to friction. On the other hand, the static ones are all the grains in the contact surface, either they participate or not in the material removal process.

3.2.1 Static Grains

Static grains are the grains that are in the grinding wheel–workpiece interface. In the past, most of the relative research studies presented attempted to calculate the number of static grains using experimental results. A number of different experimental methods can be used such as photography, photogrammetry, profilometers, etc. for the calculation of the number of static grains. Toenshoff et al. [1] based on previous studies proposed a simple empirical model for the estimation of the number of static grains

$$n_s = c \cdot z^{e2} \tag{3.1}$$

where n_s is the number of static grains, c is the specific cutting edge density, z is the profile depth and $e2$ is an empirically determined exponent. It is evident that such an approach relies on experimental results.

A simplified method for estimating the number of static grains as a function of grinding wheel specifications and process parameters was presented by Salonitis et al. [2]. By considering a finite volume including all the grains in the contact area, as it can be seen in Fig. 3.2, the number of static grains intersected by the grinding arc area can be determined. This finite volume will have its three dimensions equal to contact length, grinding wheel width and grain height. The grains

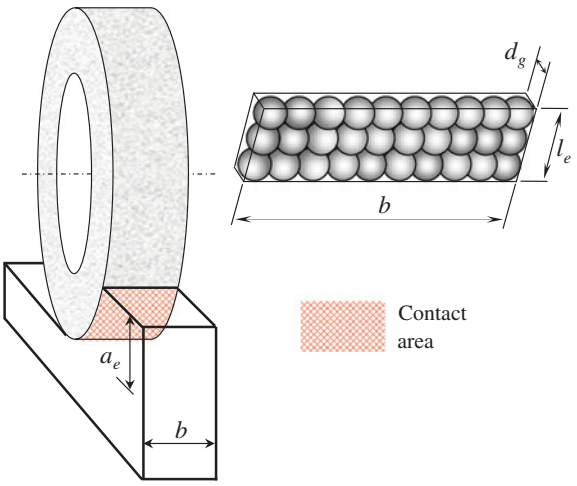

Fig. 3.2 Finite volume for the estimation of the number of the active grains

are considered spherical, thus the height of each grain will be equal to the average grain diameter. The volumetric concentration of grains in the finite volume can be determined from the following equation:

$$V_g = \frac{n_s \times V_{\text{grain}}}{V_{\text{tot}}} \tag{3.2}$$

where V_g is the volumetric concentration of abrasive grains in the grinding wheel, n_s the number of static grains, V_{grain} the average volume of each grain and V_{tot} the finite element volume.

Therefore the number of static grains can be estimated from the following equation:

$$n = 6 \cdot V_g \cdot \frac{l_c \cdot b}{\pi \cdot d_g^2} \tag{3.3}$$

where V_g is the volumetric concentration of abrasive grains in the wheel, l_c is the geometric length of contact zone ($l_c = \sqrt{d_e a_e}$), d_e is the equivalent diameter, a_e is the depth of cut, b is the grinding wheel width and d_g is the average diameter of the grains.

The volumetric concentration of abrasive grains is a function of the grinding wheel structure. The volumetric concentration of the abrasive grains, the grain diameter and the porosity of the grinding wheel are characteristics defined while it is being manufactured and its specifications are depicted qualitatively in its specifications (Fig. 3.3). Malkin [3] proposed an empirical relationship for the volumetric concentration and the grinding wheel structure number (S):

$$V_g = \frac{2(32 - S)}{100} \tag{3.4}$$

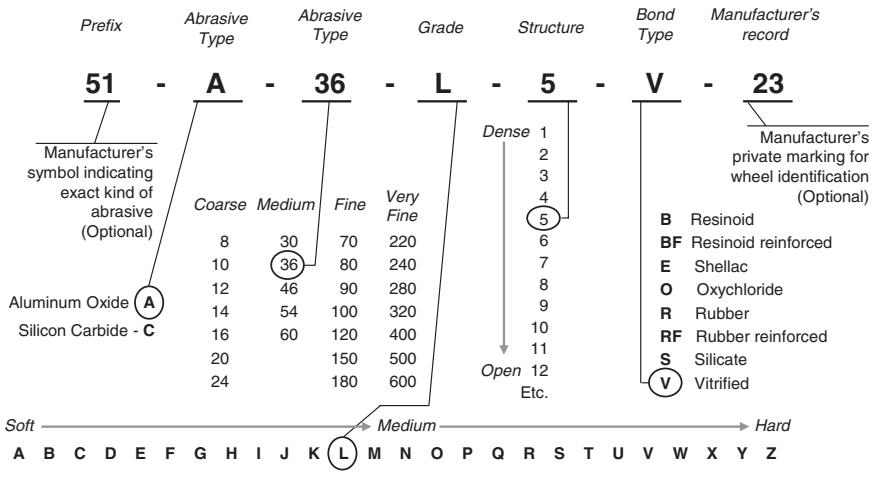

Fig. 3.3 Grinding wheel specification

The average grain diameter is correlated with the grain size number M from the grinding wheel marked with the following equation:

$$d_g = 15.2 \cdot M^{-1} \tag{3.5}$$

The above equation approximates the grit dimension d_g as 60 % of the average spacing between adjacent wires in a sieve, whose mesh number equals the grit number M.

3.2.2 Active Grains

During the grinding process, only a small number of grains are contacting and interacting with the workpiece material. This fraction of static grains is characterized as "active" or "kinematic" grains, and can be determined from the following equation.

$$n_a = \Phi_a \cdot n \tag{3.6}$$

where Φ_a is the fraction of static grains that are active.

The fraction of static grains that are active depends on a number of factors, such as the elasticity and the deformation of the grinding wheel, as well as of the workpiece during the grinding process, etc. The volumetric concentration of the bonding material on the grinding wheel can be considered as a metric of this fraction, since this parameter greatly affects the elasticity of the grinding wheel.

Since a grinding wheel is composed of grains, bonding material and air (as internal pores), the volumetric concentration of bonding (V_b) can be estimated from the following equation:

$$V_b = 1 - \left(V_g + V_p\right) \tag{3.7}$$

The volumetric concentration of grains (V_g) can be estimated from Eq. (3.4). The volumetric concentration of the pores (V_p) is a function of the "hardness" number of the grinding wheel, and the following equation can be used [3].

$$V_p = \frac{1}{100}\left(45 + \frac{S - 2n}{1.5}\right) \tag{3.8}$$

where n is an integer ($n = 1, 2, 3, 4, \ldots$) corresponding to the hardness letter (E, F, G, H, …), respectively. The above equation is valid for grinding wheels having $V_g \leq 60$ %.

For extracting the relationship between the fraction of the active grains and the volumetric concentration, the experimental data stated in [4, 5] were used. Based on a reference fraction of active grains and the experimental dependence of the number of active grains on the volumetric concentration of bonding material V_b (Fig. 3.4) a normalized factor was introduced.

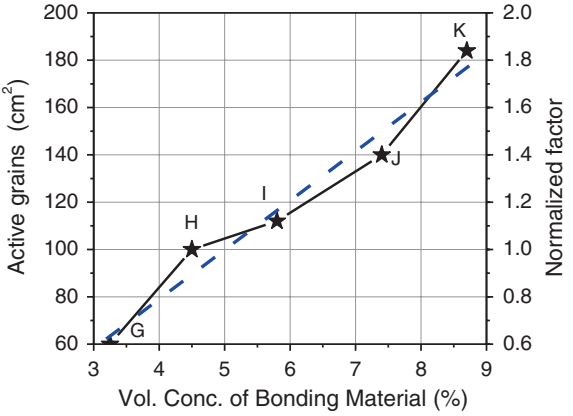

Fig. 3.4 Variation of the number of active grains per unit area with the volumetric concentration of bonding material (based on experimental data from [4])

$$(\text{normalized factor}) = 20.535 \cdot V_b - 0.217 \tag{3.9}$$

The fraction active grains can therefore be determined by the following equation:

$$\Phi_a = \Phi_{\text{ref}} \times (\text{normalized factor}) \tag{3.10}$$

For the definition of the reference fraction the results of Hou and Komanduri [5] have been used. Based on the statistical distribution of abrasive grains to the surface of a grinding wheel and the loading conditions, they have shown that although the number of grains passing through the grinding zone may be a million or more per second, the actual contacting grains are only a small fraction of those (~3–4 %) and the actual cutting grains are even less (~0.15 %). This result was obtained for a conventional alumina wheel A46H8V, and thus, the proposed model for estimating the fraction of grains that are active was calibrated for bonding material H, and fraction 3.8 %. For assessing this reference value, in the same paper, in the case of a high material removal rate grinding process, the fraction of the active grains was estimated to be 18 % (for grinding A24R6B). The proposed model, for such wheel specifications, estimates the fraction to be 19.5 %.

The approach presented is based on both existing experimental results and a simplified representation of the grinding wheel structure. Additionally, a number of empirical models for describing the topography of the grinding wheels have been presented in the past. Toenshoff et al. [1] combined these models and presented a generic equation:

$$N_{\text{kin}} = c_{gw} \cdot \left(\frac{1}{q}\right)^{e1} \cdot a_e^{e1/2} \cdot \left(\frac{1}{d_{eq}}\right)^{e1/2} \tag{3.11}$$

where N_{kin} is the number of active grains, c_{gw} is a constant for the grinding wheel effect, $e1$ is an experimentally determined exponent, q is the speed ratio, a_e is the depth of cut and d_{eq} is the equivalent diameter of the grinding wheel.

3.3 Process Forces Semi-empirical Modelling

The grinding forces can be analyzed into a tangential (F_t) and a normal component (F_n). Alternatively, grinding forces can also be described by their horizontal (F_h) and vertical (F_v) components as can be seen in Fig. 3.5. Since the diameter of the grinding wheel is much larger than the depth of cut, the horizontal component can be assumed to be identical to the tangential one.

The total grinding force can be represented as the sum of the grinding force exerted for the chip formation, for the plastic deformation (plowing) of the workpiece and for the sliding of the grinding grains on the workpiece surface.

$$F_t = F_{t,sl} + F_{t,ch} + F_{t,pl} \tag{3.12}$$

where $F_{t,sl}$, $F_{t,ch}$ and $F_{t,pl}$ are the tangential force for sliding, for chip formation and for plowing, respectively. The cutting forces include the forces exerted for chip formation and plowing:

$$F_c = F_{t,ch} + F_{t,pl} \tag{3.13}$$

3.3.1 Sliding Forces

Malkin [3], based on experimental results, has correlated the sliding forces with the friction coefficient between the workpiece material and the grinding wheel, the average contact pressure and the area of contact:

$$F_{t,sl} = \mu \cdot p_m \cdot A_a \tag{3.14}$$

where μ is the friction coefficient between the workpiece material and the abrasive grains, p_m is the average contact pressure of the abrasive grains on the workpiece and A_a is the actual area of contact between the abrasive grains and the workpiece.

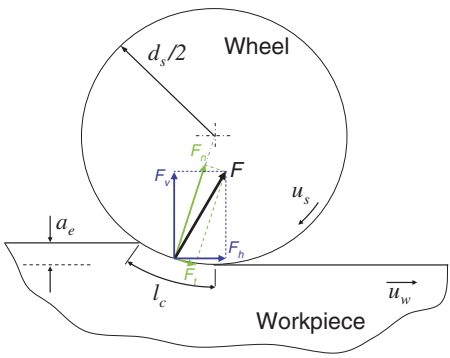

Fig. 3.5 Relationship between grinding force components

3.3.1.1 Average Contact Pressure

Malkin [3] has conducted a number of experiments with various grinding wheels and different process parameters and has proved that the average contact pressure depends solely on the cutting curvature difference.

The average contact pressure p_m is usually experimentally defined. Assuming that there is a linear relationship between curvature difference Δ and average contact pressure p_m (Fig. 3.6):

$$p_m = k_1 \Delta + k_2 \tag{3.15}$$

The cutting curvature difference Δ characterizes the degree of non-conformity between the wheel radius and the cutting path radius. Its value is strongly dependent both on the peripheral speed of the grinding wheel and the workpiece speed. When the peripheral grinding wheel speed u_c is significantly larger than the workpiece speed u_w, as for the case of the grind-hardening process, the curvature difference can be expressed as [3]:

$$\Delta = \frac{4\upsilon_w}{d_e \upsilon_c} \tag{3.16}$$

Thus the average contact pressure can be estimated by:

$$p_m = k_1 \frac{4u_w}{d_e u_s} + k_2 \tag{3.17}$$

where d_e is the equivalent diameter, and k_1 and k_2 are linear coefficients that are experimentally defined and can be considered to be a function of processing environment (grinding machine, coolant type, etc.).

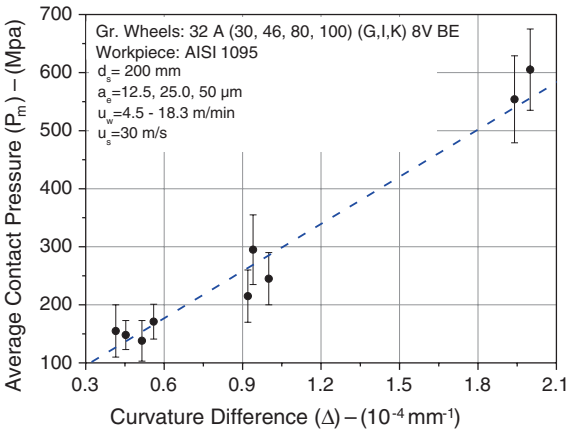

Fig. 3.6 Average contact pressure as a function of curvature difference (based on experimental results presented by Kannapan and Malkin [6])

3.3.1.2 Actual Area of Contact

The actual area of contact between the grains and the workpiece depends on the process parameters and on the grinding wheel composition. The specification of a grinding wheel describes comprehensively its composition as can be seen in Fig. 3.3.

It is assumed that the heat is generated only between the grains and the workpiece material. Therefore, the actual area of contact is the product of the number of active grains n_a adjacent to the workpiece surface and the average wear flat area A_g per grain.

$$A_a = n_a \cdot A_g \tag{3.18}$$

The average wear flat area is considered to be equal to that of a circle having diameter l_{wf} equal to the two-thirds of the average grain diameter (Fig. 3.7):

$$A_g = \frac{1}{4}\pi l_{wf}^2 = \frac{\pi d_g^2}{9} \tag{3.19}$$

3.3.1.3 Friction Coefficient

Friction coefficient is usually related to the grinding force ratio (λ) that links the normal component of the grinding forces with the tangential ones. The force ratio depends on grinding parameters, grinding wheel condition, work material, etc. For a sharp wheel, it is relatively low, as tangential force component is higher compared to normal force and for dull wheel it is opposite. The ratio of the sliding components of the forces is equal to friction coefficient (μ) between wear flat and work. Similarly, the ratio of the cutting components (φ) depends on tip angle of grain [3]. Therefore, the grinding force ratio can be expressed using the following equation [7]:

$$\lambda = \varphi \frac{F_{n,c}}{F_n} + \mu \frac{F_{n,s}}{F_n} \tag{3.20}$$

Grinding force ratio depends on both φ and μ, however, when the chip formation is more dominant than sliding; φ will be governing the force ratio. Similarly, if

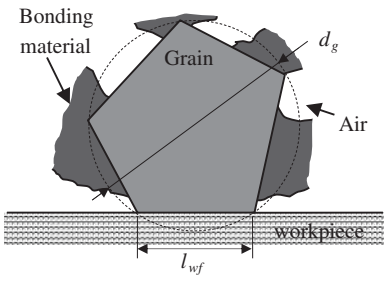

Fig. 3.7 Grain–material interaction

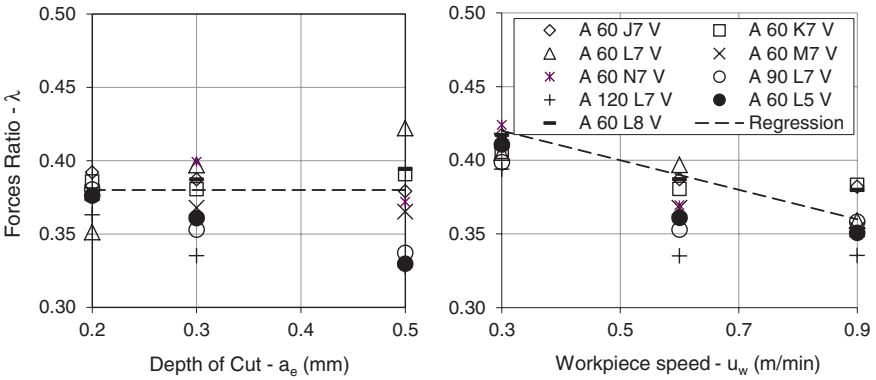

Fig. 3.8 Forces ratio dependence on depth of cut and workpiece speed (based on [2])

sliding is more dominant then μ will have more dominance grinding force ratio [8]. Therefore, for the case of grind hardening it is safe to assume that the force ratio equals the friction coefficient.

Salonitis et al. [2] derived both theoretically and experimentally that force exerted due to chip forming and plowing is negligible (less than 3 % of the total forces) in comparison to the sliding force, supporting further the validity of the assumption to use the force ratio for assessing the friction coefficient. Their experimental work on grind hardening using different alumina grinding wheels indicates that there is a strong dependence of force ratio to the workpiece speed, whereas the depth of cut change impact is not so significant (Fig. 3.8).

3.3.1.4 Sliding Forces

Combining the above-mentioned equations, the tangential grinding forces due to the grits sliding on the workpiece can be estimated using the following closed equation:

$$F_{t,sl} = \frac{3}{100 \times 15.2^2} \mu \cdot \Phi_a \cdot b \cdot l_{wf}^2 \cdot M^2 (32 - S) \sqrt{d_e \cdot a_e} \left[k_1 \frac{4u_w}{d_e \cdot u_s} + k_2 \right] \quad (3.21)$$

3.3.2 Cutting Forces

The cutting forces can be determined from the specific energy which is defined as the energy expended per unit volume of material removed. The specific energy is given by the following equation:

$$u_c = \frac{F_{t,c} \cdot u_s}{b \cdot a_e \cdot u_w} \quad (3.22)$$

where u_c is the specific cutting energy and $F_{t,c}$ is the sum of chip formation and plowing forces.

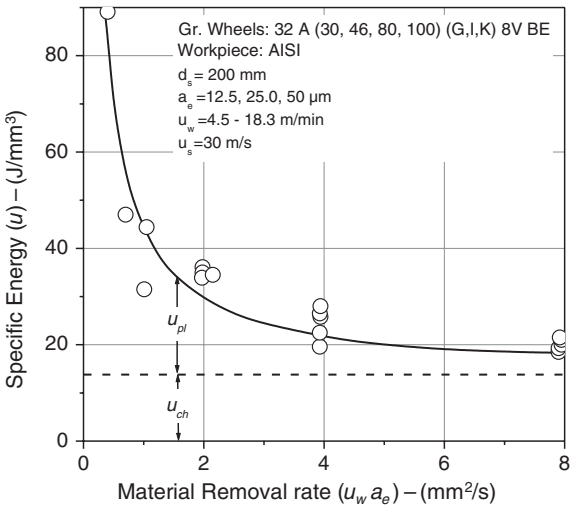

Fig. 3.9 Specific energy as a function of material removal rate (based on [3])

The cutting energy is the sum of the chip formation and the plowing energy. It has been shown [3] that the cutting energy asymptotically approaches the chip formation energy as the metal removal rate is increased (Fig. 3.9). Furthermore, it has been proven experimentally that the chip formation energy has a constant value that does not depend on the process parameters, the grinding wheel specifications or the workpiece material. Almost all the relevant studies have indicated an indicative value of specific cutting energy being equal to 13.8 J/mm^3.

Based on the experimental results presented in [3], the following equation can be drawn:

$$u_c = u_{ch} + u_{pl} = u_{ch} + \frac{28.1}{u_w a_e} \tag{3.23}$$

From Eqs. (3.22) and (3.23), the cutting forces can be estimated using the following closed format equation:

$$F_{t,c} = F_{t,ch} + F_{t,pl} = b \cdot a_e \left(\frac{u_s}{u_w}\right)^{-1} \left[u_{ch} + \frac{28.1}{u_w a_e}\right] \tag{3.24}$$

3.3.3 Model Implementation and Validation

Salonitis et al. [2] validated the model for the grind hardening of AISI 52100 for a number of different alumina grinding wheels. They concluded that cutting forces account typically for less than 3 % of the total forces (Fig. 3.10). Thus the tangential component of the process forces (Eq. 3.12) can be considered equal to the sliding component (Eq. 3.19) neglecting the cutting forces.

The process parameters and the grinding wheel specifications have an important impact on the grinding forces, indicatively in Fig. 3.11a their effect as predicted

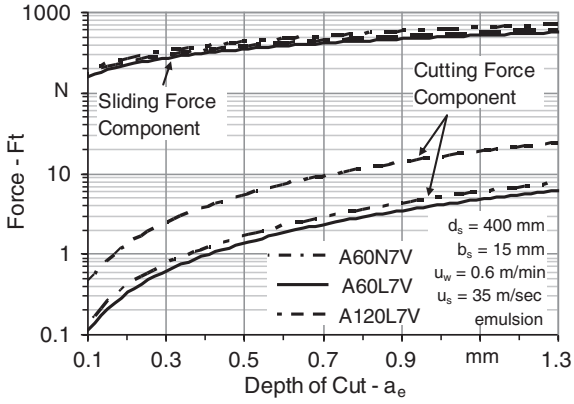

Fig. 3.10 Sliding and cutting forces versus depth of cut [2]

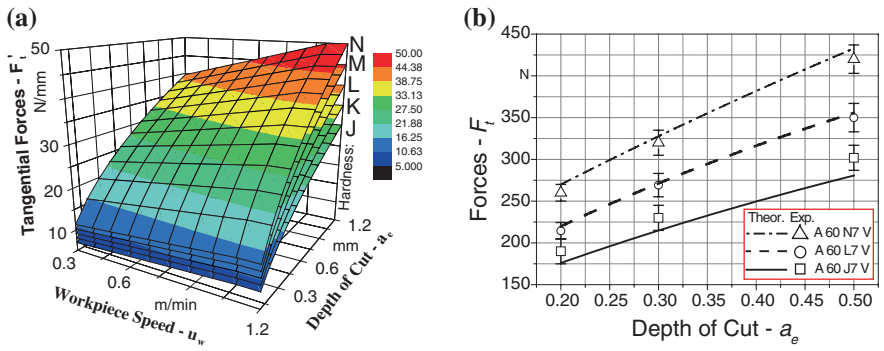

Fig. 3.11 **a** Tangential forces prediction as function of process parameters and grinding wheel structure and **b** experimental verification [2]

is shown in the model. Salonitis et al. [2], experimentally proved the models prediction and shown that the depth of cut has a significant effect on the process forces (Fig. 3.11b). The key specification characteristic was determined to be the grinding wheel hardness.

3.4 Modelling Heat Generation and Partition

As it has been noted, grind-hardening process relies on the selection of a proper set of parameters that can result in high heat generation rates in the grinding area. The heat generated should be adequate for the workpiece material to undergo heat

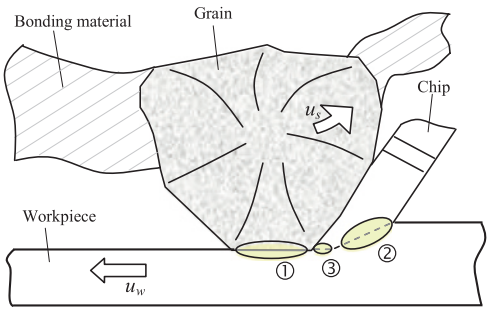

Fig. 3.12 Heat generation mechanisms during grinding

① Heat generation due to friction
② Heat generation due to plastic deformation
③ Heat generatio due to plowing

treatment and increase finally its surface hardness. In common grinding processes, the primary goal is the reduction of the generated heat and even more important the reduction of the heat entering the workpiece material as to avoid damaging the lattice structure of the material. It is evident that in grind hardening, we have the opposite goal: generating high heat flux rates and disseminate locally in the workpiece material.

During the grind-hardening process the heat generation mechanisms, as shown in Fig. 3.12, are:

- the friction among abrasive grains and workpiece material (wear flat),
- the plastic deformation in shear planes during material removal and
- the plastic deformation of workpiece material without material removal (plowing)

The dominant heat generation mechanism is that of the friction among abrasive grains and workpiece material while the other two have significantly less contribution. Lavine [9, 10] studied the heat generation due to plastic deformation in shear planes and revealed that no significant error is expected if neglected in the case of dull wheels, such as the ones used for grind-hardening applications. Malkin [3] on the other hand, proved that for grinding operations with very high removal rates, as is the case of grind hardening, the magnitude of the plowing energy is negligible in comparison with that of the heat generated by friction and the heat consumed for chip formation.

The actual amount of heat generated during the process equals to the grinding wheel spindle power:

$$P = F_t \cdot (u_s \pm u_w) \tag{3.25}$$

where P is the grinding wheel spindle power, F_t is the tangential component of the cutting forces, u_w is the workpiece speed and u_s is the grinding wheel speed. The plus sign is considered for up-grinding processes whereas the minus sign for

down-grinding processes. Since during grind hardening, the grinding wheel speed is much higher than that of the workpiece, the above equation can be simplified to:

$$P = F_t \cdot u_s \tag{3.26}$$

3.4.1 Heat Partition

The heat generated is transferred to the workpiece, grinding wheel, chips, coolant and surrounding environment. The heat transferred to the surrounding environment, due to irradiation, is considered negligible when compared to the heat dissipated to other heat sinks involved in the heat balance. Furthermore, the heat transferred through the coolant fluid can also be considered negligible as the coolant fluid cannot easily enter the grinding zone given that the grinding wheel rotates towards the fluid flow (Fig. 3.13) [11]. Additionally, even if some amount of coolant fluid enters the grinding zone, it will boil immediately since the temperature of the workpiece surface in this region exceeds 900 °C [12], and therefore, the maximum heat that could be convected by this fluid is the heat required to boil the fluid [13].

It can be argued therefore that the heat generated, due to grinding wheel—workpiece interaction, is dissipated to the workpiece, grinding wheel and the chips (Fig. 3.14). This heat balance can be expressed in terms of heat fluxes as:

$$q_t = q_w + q_s + q_{ch} \tag{3.27}$$

where q_t is the heat generation flux and q_w, q_s and q_{ch} are the amounts of heat convected by the workpiece, the grinding wheel and the chips, respectively.

The heat generation flux can be calculated from the power consumed during the process.

$$q_t = \frac{P}{b \cdot l_c} \tag{3.28}$$

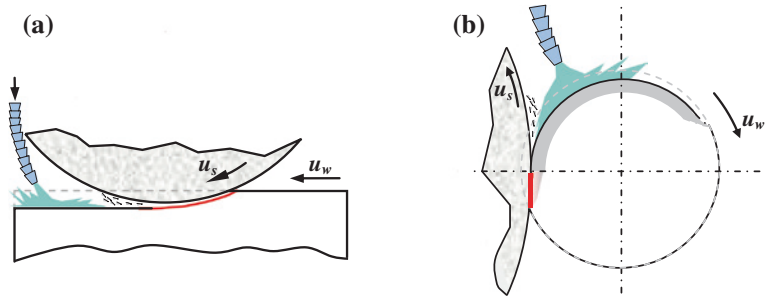

Fig. 3.13 Coolant fluid application during grind-hardening process for **a** prismatic and **b** cylindrical workpieces

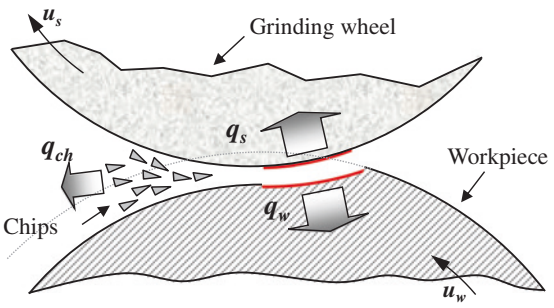

Fig. 3.14 Grinding heat transfer to workpiece (q_w), to chips (q_{ch}) and to grinding wheel (q_s)

where b is the grinding wheel width and l_c is the geometrical contact length between the workpiece and the grinding wheel:

$$l_c = \sqrt{a_e \cdot d_e} \tag{3.29}$$

where d_e is the equivalent diameter and a_e is the depth of cut. However, the geometric contact length is an underestimation of the real contact length. The shape of the contact area is deformed, due to the elastic and plastic behaviour of the wheel and the workpiece system. Experimentally, it has been shown that the actual contact length can be 50–200 % greater than the geometrical contact length [14, 15]. For the purposes of the present work though, the geometrical contact length will be used, since no analytical expressions of the actual contact length have been derived for the case of high material removal rate grinding processes such as the grind hardening.

The amount of heat transferred by the various "sinks" (grinding wheel, workpiece, chips, coolant, etc.) is of great interest for the process modelling. In the literature, a number of theoretical models have been presented, that can be classified in two major categories (Fig. 3.15):

- "grain" models, in which the analysis takes place at the interaction plane between the grinding wheel grit and the workpiece material (most of these models are based on Lavine et al. [16] work, indicative studies include the work by Rowe et al. [13, 17–20], Guo and Malkin [21–24], and
- "grinding zone" models, in which the analysis takes place at the interface between the grinding wheel and the workpiece (typical examples of such models include the works by Jin et al. [25], Toenshoff et al. [26], Rowe et al. [17, 20, 27].

For the grind-hardening process modelling, a grinding zone model is adapted due to higher simplicity and experimental verification of the results in a number of publications [11, 28, 29].

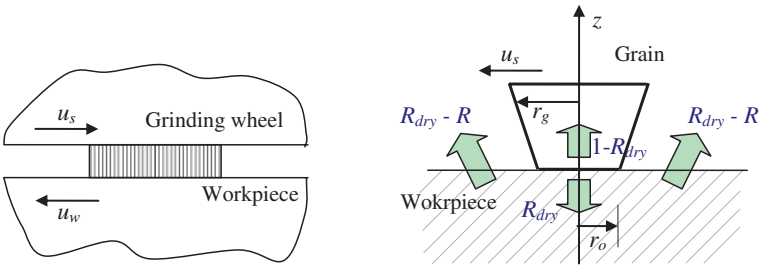

Fig. 3.15 Heat partition models formulation

3.4.2 Heat Dissipation by the Chips

As aforementioned, heat is dissipated with process chips. In case of shallow grinding, this amount of heat can be neglected; however, for high material removal rates [30], as is grind hardening, this heat dissipation should be taken into consideration. The heat flux convected by the chips can be expressed as a function of specific energy distributed over the grinding zone:

$$q_{ch} = e_{ch} \cdot \frac{a_e \cdot u_w}{l_c} \tag{3.30}$$

where e_{ch} is the specific energy convected by chips, a_e is the depth of cut, u_w is the workpiece speed and l_c is the geometric contact length

The chip temperature may easily reach the melting point as argued by Malkin [3]. Therefore, the maximum specific energy convected by the chips can be assumed to equal the required energy for raising the temperature of the chip to the melting point:

$$e_{ch} = \rho_{w,T=Tmp} \cdot c_{w,T=Tmp} \cdot T_{mp} \tag{3.31}$$

where T_{mp} is the melting point.

The ratio of the heat flux partition to chips can be therefore estimated by the heat flux convected by the chips and the total heat flux generated.

$$R_{ch} = \frac{q_{ch}}{q_t} \tag{3.32}$$

3.4.3 Heat Dissipation by the Grinding Wheel

The partition of the heat between the workpiece and the grinding wheel has been thoroughly investigated. Malkin [3], Lavine [9], Rowe [13, 20, 30, 31] and Jin et al. [25] are few of the researchers that studied this subject. The partition ratio R_{ws} is defined as the fraction of the heat shared by the workpiece and the grinding wheel entering the workpiece.

$$R_{ws} = \frac{q_w}{q_w + q_s} \tag{3.33}$$

The partition ratio in earlier grinding studies was approached based on heat transfer models that compared the grinding process to that of machining and the grains were thought of as machine tools. Most of these models were based on Hahn's [32] preliminary modelling work that partitioned the heat between the grain and the workpiece. However, in machining, the majority of the heat is generated at the shear plane and the heat enters the tool through the tool–chip interface. Since in grinding, most of the heat is generated by friction at the grain–workpiece interface, and the contact area is much larger, the simplified heat partitioning model developed by Rowe et al. [20], which assumes that the grinding wheel and the workpiece can be thought of as two sliders, seems to better simulate the heat transfer during grinding. The aforementioned partition model is utilized for the present study:

$$R_{ws} = \left(1 + \frac{\beta_s}{\beta_w} \cdot \sqrt{\frac{u_s}{u_w}}\right)^{-1} \tag{3.34}$$

where factor β_w is the coefficient of heat diffusion of the workpiece and factor β_s is the average heat coefficient of the grinding wheel defined, respectively, as:

$$\beta_w = \sqrt{k_w \cdot \rho_w \cdot c_w} \tag{3.35}$$

$$\beta_s = \sqrt{\bar{k}_s \cdot \bar{\rho}_s \cdot \bar{c}_s} \tag{3.36}$$

where k, ρ and c are the average values of thermal conductivity, density and specific heat of the workpiece or the respective effective values of the grinding wheel for a temperature equal to that of the contact zone.

A number of attempts have been reported having focused on determining the effective properties of the grinding wheel. Rowe et al. [20] attempted to measure experimentally the coefficient of the heat diffusion. Kim et al. [33] simulated the grinding wheel, in the grinding zone, as a thermal composite consisting of abrasive grains and fluid between them. They used the "law of mixtures" for determining the effective properties. The thermal composite body is considered to be consisted of grains and air between them, since no cooling fluid enters the grinding zone during the grind-hardening process [28]. Using the "law of mixtures", the effective thermal properties can be determined by equation:

$$\bar{i}_s = \varphi \cdot i_g + (1 - \varphi) i_a \tag{3.37}$$

where i_s is the effective value of the property of the thermal composite (density, thermal conductivity and specific heat), i_g and i_a are the properties of the grain and the air, respectively. Finally, φ is the surface density of the thermal composite.

The surface density is a means of estimating the concentration of active grains on the surface of the grinding wheel. The volumetric concentration of grains on the grinding wheel that can be estimated by using the empirical relations

presented, is quite higher than that on the surface, since no differentiation exists between the active and static grains and thus, cannot be used for estimating the effective thermal properties. The surface density of the grinding wheel can be determined as the fraction of the real contact area to the total surface area:

$$\varphi = \frac{A_a}{l_c \cdot b} \tag{3.38}$$

where A_a is the real contact area determined from the total number of active grains and the wear flat area, l_c is the length of the arc contact and b is the width of the grinding wheel.

3.4.4 Heat Entering the Workpiece

Once the heat partition ratio among the grinding wheel and the workpiece and the heat flux dissipated by the grinding chips have been determined, the heat flux entering the workpiece can be derived by combining Eqs. 3.27 and 3.33 as:

$$q_w = R_{ws} \cdot (q_t - q_{ch}) \tag{3.39}$$

The heat partition to the workpiece and the grinding wheel can therefore be estimated from the following equations

$$R_w = \frac{q_w}{q_t} \tag{3.40}$$

$$R_s = \frac{q_s}{q_t} \tag{3.41}$$

3.4.5 Model Implementation and Validation

The model proposed for the heat partition has been validated for the case of dry grind hardening of AISI 52100 and AISI 1045. In grind hardening the grinding wheel speed is many times higher than the workpiece speed. The speed ratio (u_s/u_w) is usually in the range of 1,000–8,000. Thus for the case of grind hardening with a corundum grinding wheel of a workpiece made of AISI 52100, the heat that enters the workpiece lies between 48 and 63 %. Similar findings are noted for AISI 1045 as well. As a comparison, for conventional finish grinding process (with depth of cut between 0.005 and 0.050 mm and a speed ratio less than 40), the heat partition ratio is between 75 and 90 %. The use of CBN wheels could reduce significantly the heat partition ratios (30–50 %), since CNC grits present higher thermal conductivity and thus absorb more heat.

Using the heat partition model described, the heat partition to the chip, the workpiece and the grinding wheel as a function of workpiece speed and depth of cut was calculated and presented in Fig. 3.16. The heat that enters the workpiece

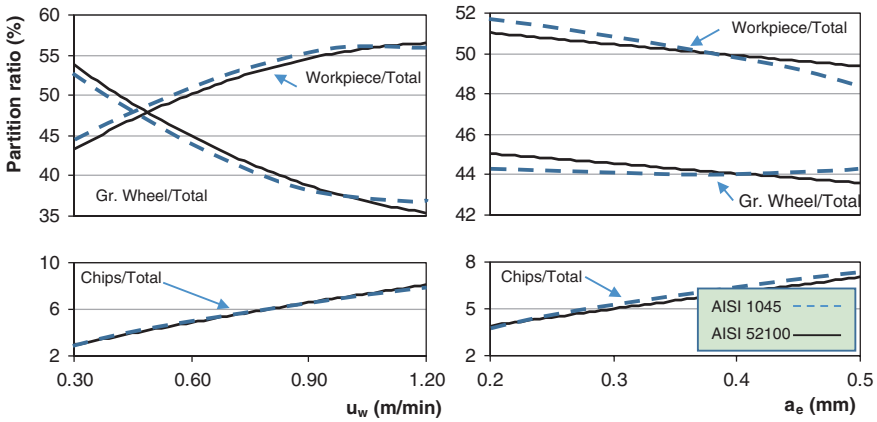

Fig. 3.16 Heat partition ratio **a** $u_w = 0.60$ m/min, **b** $a_e = 0.3$ mm ($u_s = 35$ m/s, grinding wheel: A 60 L7V)

is in the range of 40–60 % of the total generated heat. The portion of heat entering the workpiece increases with the increase of the workpiece speed. Increasing the depth of cut, results in the slight reduction of portion of the heat that enters the workpiece.

It can be thus concluded that most of the heat generated is shared between the workpiece material and grinding wheel, with only a small portion rejected with the grinding chips (with a maximum portion of 10 %). Comparing to other high material removal rates, during high efficiency deep grinding (HEDG) most of the heat is dissipated through chips [34] whereas for the case of creep feed grinding, up to 80 % of the heat is dissipated by the cutting fluid and only 3–4.5 % is conducted within the workpiece material [33].

3.5 Modelling of Temperature Distribution

Having determined the amount of heat entering the workpiece, the next step is to calculate the temperature distribution within the workpiece material. A number of theoretical models have been presented for the estimation of the temperature field in grinding [13, 16, 22, 23, 35–39], that are based on the "moving heat source" model developed by Carslaw and Jaeger [40].

The driving equations are different based on whether the modelling of the process is on prismatic or cylindrical workpiece geometries. Furthermore, the use or not of a coolant fluid affects the boundary conditions. A common characteristic of both models presented hereafter is that since the heat source width is quite larger than the heat penetration depth, they are modelled in two dimensions with infinite length.

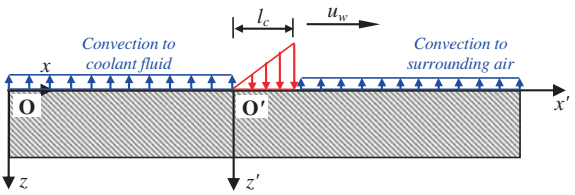

Fig. 3.17 A theoretical temperature model of grind hardening for prismatic workpieces

3.5.1 Modelling of Prismatic Workpiece Geometries

The basic theoretical model for estimating the temperature distribution in prismatic workpieces is shown in Fig. 3.17. A workpiece of finite dimensions is considered. The heat source moves along the positive direction of the x-axis on the workpiece surface with a constant velocity u_w. The coordinate system x′Oz′ is fixed at the start of the heat source and moves along with it. The global coordinate system xOz is fixed to the workpiece and coincides with the moving coordinate system at the instant $t = 0$.

For modelling purposes, the grinding process is assumed to be quasi-stationery and therefore, the temperature field is the solution to the following differential equation:

$$\frac{\partial^2 T}{\partial x^2} + \frac{\partial^2 T}{\partial z^2} + \frac{u_w}{a_w}\frac{\partial T}{\partial x} = 0 \tag{3.42}$$

where T is the temperature rise relative to the ambient temperature T_o and a_w is the thermal diffusivity of the workpiece material. The boundary conditions the solution should follow are defined by the heat source and the heat convection to the air and the coolant fluid (if used). The initial condition for solving the differential equation is:

$$T(x, z)|_{t=0} = T_o \tag{3.43}$$

The heat source distribution affects the calculated temperature filed. A number of different distribution models have been presented in the literature as can be seen in Fig. 3.18.

For the case of grind hardening, the heat source distribution is assumed to present triangular distribution over the contact length, with its peak being at the direction of movement. It has been proven experimentally that the heat generation rate is proportional to the rate of material removal [30]. Since the material removal rate varies linearly across the contact zone with its maximum value at the direction of movement, it is safe to assume that the heat flux distribution will present its peak at the leading edge of the contact zone. The above argument can be also justified by the chip geometry according to Jin and Cai [41]. Temperature predictions, using a triangular heat source distribution, have also been found to be more consistent with temperature measurements in the

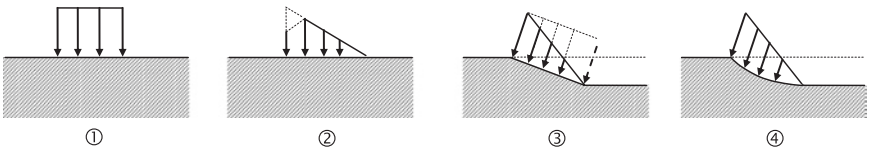

Fig. 3.18 Heat source distribution models: *1* Top hat, *2* Triangular, *3* Inclined and *4* Triangular on an arc contact length

workpiece sub-surface during a grinding pass [20]. Therefore, the heat source is expressed by the following equation:

$$q(x') = \begin{cases} \frac{q_w}{l_c} x', & 0 \le x' \le l_c,\ z = 0 \\ 0, & x' \le 0 \text{ and } x' \ge l_c,\ z = 0 \end{cases} \tag{3.44}$$

3.5.1.1 Dry Grind Hardening

Grind hardening, at least initially, was performed without the use of a coolant fluid. In that case the heat is transferred to the surrounding through convention everywhere besides the area where the heat source lies. The boundary conditions in that case can be described through the following equations:

$$\begin{cases} k_w \frac{\partial T}{\partial z}\Big|_{z=0} = \begin{cases} q(x'), & 0 \le x' \le l_c \\ -h_a\big(T(x') - T_o\big), & x' \le 0 \text{ or } x' \ge l_c \end{cases} \\ T \to T_o,\ \frac{\partial T}{\partial x},\ \frac{\partial T}{\partial z} \to 0, \quad \text{when } z, x \to \infty \end{cases} \tag{3.45}$$

where h_a is the heat transfer coefficient to the surrounding air.

3.5.1.2 Wet Grind Hardening

In order to better understand the need and usage of the coolant fluid during grind hardening, the process will be compared with that of the creep feed grinding, which presents many similarities. Both processes are characterized by very slow workpiece speeds and extremely large cut depths. However, the friction heat generated due to these process characteristics can either be catastrophical in the case of creep feed grinding or beneficial in the case of grind hardening. In the case of creep feed grinding, the heat generated is removed with the aid of a copious supply of cutting fluid delivered, at high pressure, to the grinding zone. On the other hand, in the case of grind hardening, the heat generated is dissipated inside the workpiece so as to raise the surface temperature and induce metallurgical transformations. When bulky materials are grind hardened, the quenching of the workpiece is achieved by the dissipation of the heat inside the workpiece. However, for utilizing the process with thick or small diameter cylindrical parts, the cooling rate achieved is not so significant as to allow the martensitic transformation.

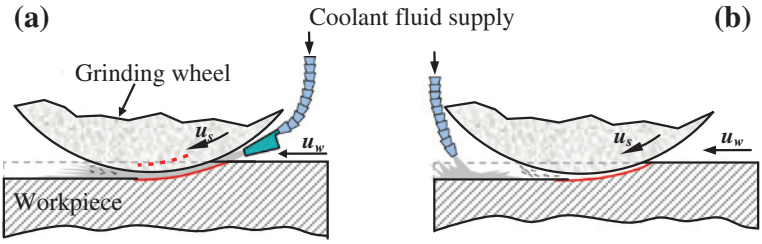

Fig. 3.19 Cutting fluid supply in the case of **a** creep feed grinding and **b** grind hardening

Therefore, the application of a coolant fluid directly after the contact area is mandatory for achieving the quenching of the part. The application of the coolant fluid also reduces the grinding wheel temperature thus, prolonging its life. Figure 3.19 compares the application of the coolant fluid for creep feed and grind-hardening operations in the case of surface workpieces.

Following the process mechanics presented in Fig. 3.19b, the boundary conditions can be derived. The heat is convected to air in front of the grinding area and to the coolant fluid behind the grinding area. Therefore, the boundary conditions of the differential Eq. 3.42 are:

$$\begin{cases} k_w \frac{\partial T}{\partial z} = \begin{cases} q(x'), & 0 \le x' \le l_c,\ z = 0 \\ -h_a T(x'), & x' \ge l_c,\ z = 0 \\ -h_f T(x'), & x' \le 0,\ z = 0 \end{cases} \\ T \to T_o,\ \frac{\partial T}{\partial x}, \frac{\partial T}{\partial z} \to 0, \quad \text{when } z, x \to \infty \end{cases} \tag{3.46}$$

where h_a and h_f are the heat transfer coefficient to the surrounding air and to the coolant fluid, respectively.

3.5.1.3 Final Cooling Stage

The grinding wheel–workpiece interaction finishes when the grinding wheel exits the workpiece. The quenching of the workpiece surface is further enhanced by a final cooling phase. Coolant fluid is amply supplied to the workpiece until its temperature drops to that of the environment. During this phase, the boundary conditions (Eqs. 3.45 or 3.46 depending on whether coolant fluid is used) are replaced by the following equation:

$$-k_w \left.\frac{\partial T}{\partial z}\right|_{z=0} = h_{f,\text{final}} \cdot \left(T(x) - T_f\right) \text{ for } t \ge l_p / u_w \tag{3.47}$$

where $h_{f,\text{final}}$ is the average heat transfer coefficient to the coolant fluid, and T_f is the cutting fluid temperature and l_p the length of the workpiece.

3.5.1.4 Temperature Distribution Calculation

The solution of the differential Eq. 3.42 with the boundary conditions provides the temperature distribution within the workpiece material. The above equations can be solved either numerically or they can be numerically approached by using FEA.

3.5.2 Modelling of Cylindrical Workpiece Geometries

The basic theoretical model for estimating the temperature distribution in cylindrical workpieces is shown in Fig. 3.20. A cylindrical workpiece with a radius r_w is considered. The heat source is assumed to be moving on the circumference of the cylinder with a constant velocity equal to that of the workpiece u_w. The polar coordinate system is fixed at the centre of the workpiece.

The differential equation that is governing the heat conduction problem is the energy equation expressed in polar coordinates:

$$\rho_w \cdot c_w \cdot \frac{\partial T}{\partial t} = k_w \cdot \left(\frac{\partial^2 T}{\partial r^2} + \frac{1}{r} \cdot \frac{\partial T}{\partial r} + \frac{1}{r^2} \cdot \frac{\partial^2 T}{\partial \theta^2} \right) \tag{3.48}$$

where ρ_w, c_w and k_w are density, specific heat and heat conductivity of the workpiece material, respectively, and r and θ is the cylindrical coordinates with $r \geq 0$ and $\theta \in [0, 2\pi)$.

The boundary conditions are defined by the heat source and the heat convection by the coolant fluid (if used) and the surrounding air. The initial condition for solving the differential equation is:

$$T(r, \theta)|_{t=0} = T_o \tag{3.49}$$

where T_o is the workpiece's initial temperature.

The heat source distribution is assumed to present triangular distribution over the contact length with its peak towards the direction of moving, as has been assumed for the case of prismatic geometries as well. It is assumed that for time

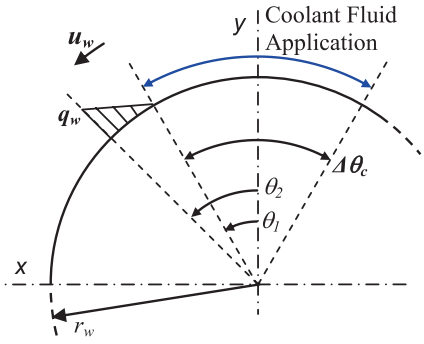

Fig. 3.20 Workpiece modelling (for simplicity only one quarter of the workpiece is presented)

$t = 0$ the heat source coincides with axis y, therefore, θ_1 determines the heat source position at an arbitrary time t. Furthermore, θ_1 and θ_2 determine the length of the heat source, as shown in Fig. 3.20, which is equal to grinding wheel–workpiece contact length. Finally, $\Delta\theta_{\text{contact}}$ determines the workpiece surface to which the coolant fluid is applied for quenching assistance.

$$\theta_1 = \omega_w \cdot t = \frac{u_w}{r_w} \cdot t \tag{3.50}$$

$$\theta_2 = \theta_1 + \Delta\theta_{\text{contact}} = \theta_1 + \frac{l_c}{r_w} \tag{3.51}$$

where ω_w is the workpiece rotational speed and l_c is the contact length between the workpiece and the grinding wheel.

The heat source triangular distribution expressed in polar coordinates is given by the following equation.

$$q(\theta) = \frac{q_w \cdot r_w}{l_c} \cdot \cos\left(\frac{\pi}{2} \cdot \frac{\theta_2 - \theta}{\theta_2 - \theta_1}\right) \tag{3.52}$$

3.5.2.1 Dry Grind Hardening

Under dry conditions (without the use of coolant fluid), the heat is transferred to the surrounding air through conduction from the workpiece surface besides the area where the heat source lies. The boundary conditions in that case can be described through the following equations:

$$-k_w(T) \cdot \left.\frac{\partial T}{\partial r}\right|_{r=r_w} = -q_w(\theta) \text{ for } \theta \in [\theta_1, \theta_2] \;\&\; t \leq 2\pi \times r_w/u_w \tag{3.53}$$

$$-k_w \left.\frac{\partial T}{\partial r}\right|_{r=r_w} = h_a(T) \cdot (T(r = r_w, \theta) - T_a) \text{ for } \theta \in [0, \theta_1) \cap (\theta_2, 2\pi) \;\&\; t \leq 2\pi \times r_w/u_w \tag{3.54}$$

where q_w is the heat source distribution, h_a is the respective coefficient between the workpiece material and the surrounding air and T_a is the surrounding air temperature. It is assumed that for time $t = 0$ the heat source coincides with axis y, therefore, θ_1 determines the heat source position at an arbitrary time t. Furthermore, θ_1 and θ_2 determine the length of the heat source, as shown in Fig. 3.20, which is equal to grinding wheel–workpiece contact length.

3.5.2.2 Wet Grind Hardening

As mentioned during the prismatic geometry model presentation, during grind hardening the coolant fluid is usually supplied directly after the contact zone

for assisting the quenching of the workpiece material. In conventional grinding processes, the coolant fluid is applied to the wedge, formed by the wheel and the workpiece through a nozzle. Another difference from conventional grinding is that during grind hardening, the coolant fluid does not enter the grinding zone since the grinding wheel rotates towards the fluid flow. Therefore, the contact zone is under dry conditions. For cylindrical grind hardening, only one quadrant of the workpiece is effectively cooled by the coolant fluid (Fig. 3.20). Thus, parameter $\Delta\theta_c$ is assumed to be equal to 90°. The boundary conditions in that case can be described through the following equations:

$$-k_w(T) \cdot \left.\frac{\partial T}{\partial r}\right|_{r=r_w} = -q_w(\theta) \text{ for } \theta \in [\theta_1, \theta_2] \;\&\; t \leq 2\pi \times r_w/u_w \tag{3.55}$$

$$-k_w(T) \cdot \left.\frac{\partial T}{\partial r}\right|_{r=r_w} = h_f(T) \cdot \left(T(r = r_w, \theta) - T_f\right) \text{ for } \theta \in [\theta_1 - \Delta\theta_c, \theta_2] \;\&\; t \leq 2\pi \times r_w/u_w \tag{3.56}$$

$$-k_w(T) \cdot \left.\frac{\partial T}{\partial r}\right|_{r=r_w} = h_a(T) \cdot (T(r = r_w, \theta) - T_a) \text{ for } \theta \in [0, \theta_1 - \Delta\theta_c) \cap (\theta_2, 2\pi) \;\&\; t \leq 2\pi \times r_w/u_w \tag{3.57}$$

where q_w is the heat source distribution, h_f is the heat transfer coefficient between the workpiece material and the coolant fluid, h_a is the respective coefficient between the workpiece material and the surrounding air, T_f is the cutting fluid temperature and T_a is the surrounding air temperature. It is assumed that for time $t = 0$, the heat source coincides with axis y, therefore, θ_1 determines the heat source position at an arbitrary time t. Furthermore, θ_1 and θ_2 determine the length of the heat source, as shown in Fig. 3.20, which is equal to grinding wheel–workpiece contact length. Finally, $\Delta\theta_c$ determines the workpiece surface to which the coolant fluid is applied for quenching assistance.

3.5.2.3 Final Cooling Stage

The grinding wheel–workpiece engagement ends once the workpiece has completed one full rotation. Afterwards, the workpiece rotates with full speed under a direct coolant flow rate until the workpiece temperature reaches environment temperature. During this phase, the boundary conditions (Eqs. 3.53–3.57) are replaced with the following equation.

$$-k_w(T) \cdot \left.\frac{\partial T}{\partial r}\right|_{r=r_w} = h_f \cdot \left(T(r = r_w, \theta) - T_f\right) \tag{3.58}$$

3.5.3 Modelling Using Finite Element Analysis

It is evident that the differential equations characterizing the grind-hardening process can be more easily solved using numerical methods or finite element methods.

In this case, the heat transfer problem (Eq. 3.42 or 3.48, depending on whether prismatic or cylindrical geometries are modelled) can be described by the following equation:

$$[C(T)]\{T\prime(t)\} + [K(T)]\{T(t)\} + \{v\} = \{Q(t)\} \tag{3.59}$$

where $[K]$ is the conductivity matrix, $[C]$ the specific heat matrix, $\{T\}$ the vector of nodal temperatures, $\{T'\}$ the vector of time derivative of $\{T\}$, $\{v\}$ is the velocity vector, which is equal to zero as no mass transport is assumed in the current problem, and $\{Q\}$ the nodal heat flow vector. Since the expected temperature is always below melting temperature, no phase change occurs and thus the enthalpy of the material does not need to be considered.

The procedure for developing and solving a finite element model for the case of grind hardening is shown in Fig. 3.21, and is identical either the geometry is considered prismatic or cylindrical. Since the heat source width is quite larger than the heat penetration depth, they are modelled in two dimensions with infinite length. The meshing of the geometry is determined by running the model a number of times, with the modelled geometry having in each run twice as many elements as in the previous run. The final meshing density can be determined when two succeeding runs presents less that 2 % difference. The elements distribution should be denser in the workpiece surface since the temperature is expected to be considerably higher in this area. Their size can be increased gradually towards the workpiece centre for the case of cylindrical geometries or as we move further away from the area of heat generation. Two typical examples of finite element models for a cylindrical and a prismatic workpieces shown in Fig. 3.22.

The heat source is considered presenting triangular heat distribution and its length being equal to the grinding wheel–workpiece geometrical contact length. The workpiece feed speed can be modelled through the movement of the heat source on the workpiece surface with a constant velocity equal to that of the workpiece feed. The heat transfer problem thus can be considered a quasistationary one. Therefore, for a finite time step, the heat source can be assumed to be static in a specific position on the workpiece surface and at the succeeding time step, the heat source will move over a length equal to the product of the workpiece speed with the time step duration. The time step duration affects the accuracy of the analysis results.

Another significant aspect of such modelling is the material properties to be considered for the workpiece material. Since the temperature exceeds in some cases 1,000 °C, it is important to consider temperature-dependent properties. The temperature dependence of the workpiece material results thus in a highly nonlinear heat transfer problem.

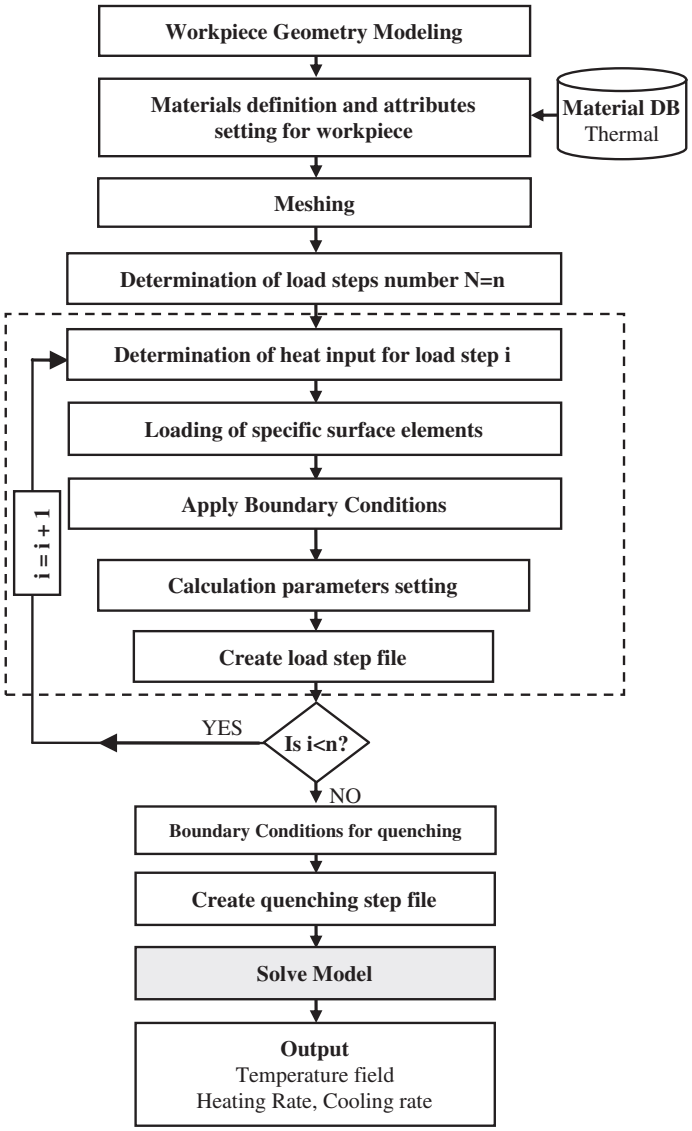

Fig. 3.21 FEA model generation and solving approach

3.5.4 Model Implementation and Validation

Following the finite element model development process outlined in Fig. 3.21, Salonitis et al. solved it for the simple case of a prismatic workpiece material [28] and cylindrical ones [11] (Figs. 3.23 and 3.24, respectively). In Fig. 3.25, the temperature as a function of heat flux and the distance below the grinding zone is shown.

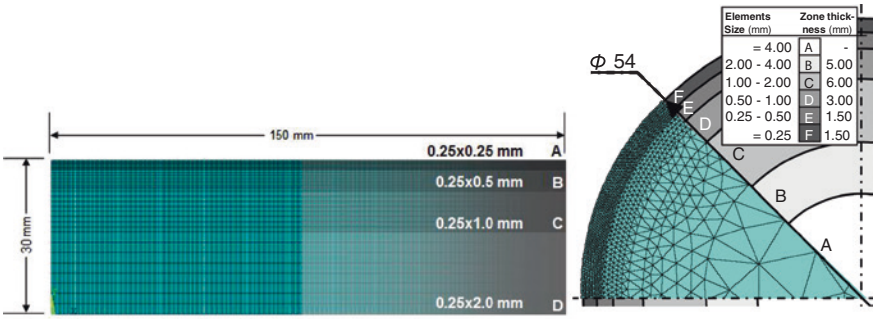

Fig. 3.22 FEA models: **a** prismatic [28] and **b** cylindrical geometry [11]

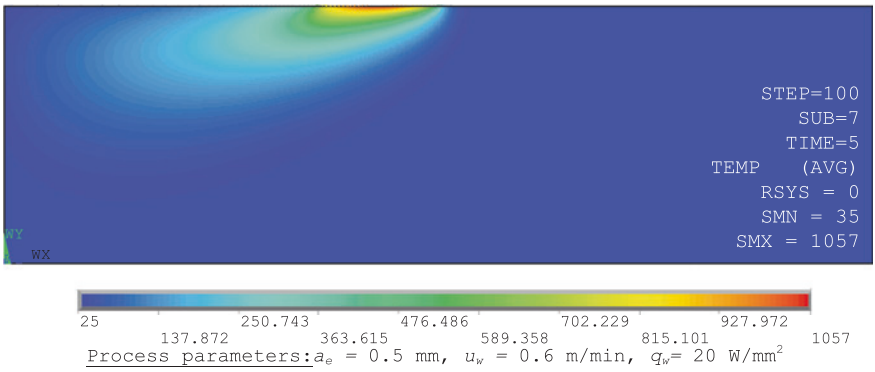

Fig. 3.23 Temperature distribution calculated using finite element models for a prismatic geometry

3.6 Modelling of Metallurgical Changes

3.6.1 Introduction Surface Heat Treatment Mechanisms

Heat treatment processes are used for the improvement of the workpiece performance under dynamic loads and friction. In their simplest form, the entire workpiece is heated above the austenitization temperature in a furnace, hold in that temperature for a specific period of time, and subsequently quenched with an appropriate medium (usually water or oil). This sequence of controlled heating and cooling alters the lattice structure within the material and as a result the surface hardness can be increased.

However, usually it is not required by the design of the component to be heat treated throughout its geometry, making thus the conventional heat treatment approaches inefficient. Instead, surface or even localized hardening is required and can be used for the production of high added value and precision components.

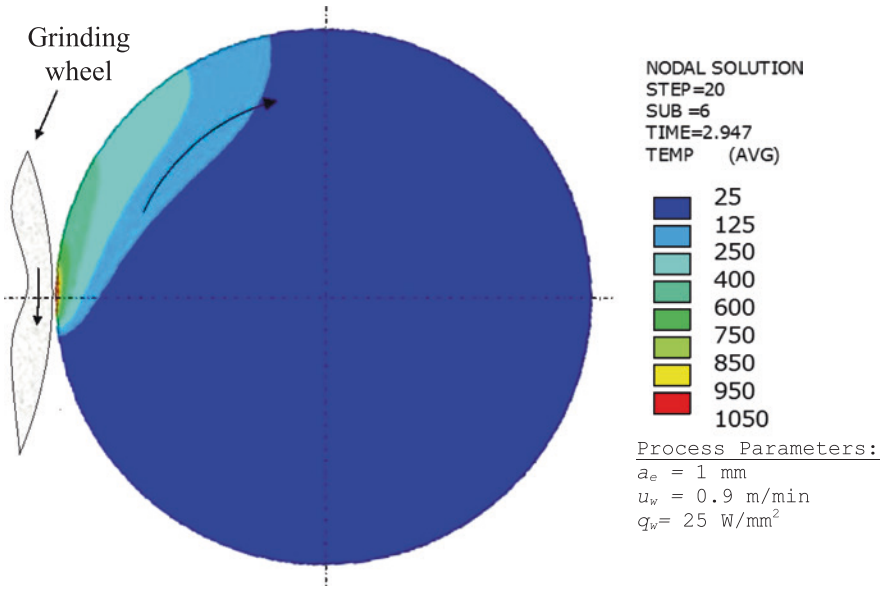

Fig. 3.24 Temperature distribution calculated using finite element models for a cylindrical geometry

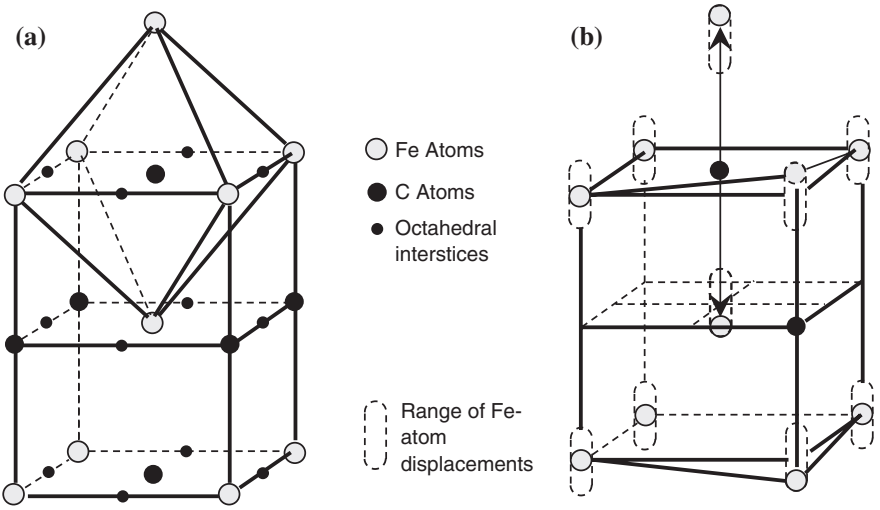

Fig. 3.25 **a** Body-centred tetragonal crystal structure of martensite in Fe-C alloys **b** iron atom displacements due to carbon atoms in martensite

Such localized surface hardening methods can prove beneficial for industry due to their advantages such as increased flexibility, reduced lead times, and reduced heat treatment deformation.

The usual methods for surface and/or local hardening can be classified into two big categories: ones with and ones without alteration of the chemical composition of the workpiece material. Indicatively, local hardening methods with simultaneous change of chemical composition are the carbonization and nitridization methods. The hardening of the component without the alteration of chemical composition is achieved through local and rapid heating of the workpiece surface with the subsequent self-quenching to the rest of the workpiece material mass. In such cases, the heating is achieved through conventional methods such as flame torches (flame hardening) or by utilizing more state-of-the-art methods such us induction coils, laser beams and electron beams. Grind hardening can be considered as one of these methods, since the heat generated in the grinding zone is the root cause for the local and rapid increase of the workpiece temperature that results in the formation of martensite.

The high hardness values observed in a steel material is due to the presence of martensite in its structure. Martensite is one of the phases that the steel can take and represents a specific lattice structure, where the carbon atoms are trapped in octahedral structure. The key reason that the martensite structure is characterized by high strength and hardness is due to the trapped carbon atoms [42] that result in displacements of iron atoms in the body-centred crystal structure (Fig. 3.25). Such deformation of the crystal structure prohibits the displacement of deformations, increasing thus the strength and hardness of steel.

Martensite's origin is austenite. When a steel material is heated above the austenitization temperature, carbon atoms have increased mobility and can freely move within the crystal structure. If the steel is cooled down with slow rates, the carbon atoms through diffusion have enough time to return to pre-austenitization phases such as ferrite and cementite. However, if the cooling is rapid, diffusion is prohibited and austenite is transformed to martensite. Since this martensitic transformation is diffusionless, the martensite has exactly the same composition as does its parent austenite. The carbon atoms do not partition themselves between cementite and ferrite but instead are trapped in the octahedral sites of a body-centred tetragonal unite cell (Fig. 3.25a).

The cooling rate of the austenite structure is critical and determines the lattice crystal structure that will be formatted during the quenching. As it has been described, depending on the cooling rate, the austenite structure can be transformed in various crystal structures such as ferrite, cementite, perlite, bainite and martensite. The effect of a specific cooling rate on the crystal structure is depicted in the CCT diagram (Fig. 3.26).

In Fig. 3.26, two diagrams are presented, the Isothermal Transformation (IT) with dashed lines and the Continuous Cooling Transformation (CCT) with continuous lines. These lines define the beginning and the end of specific transformations when the cooling curve of the workpiece material passes through these areas. The key difference between IT and CCT diagrams lies in the cooling

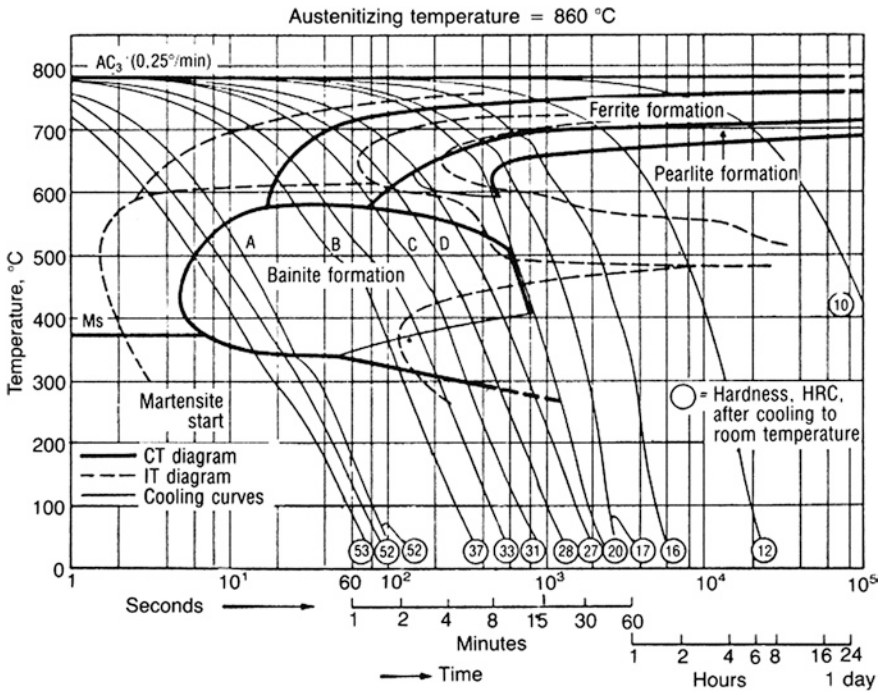

Fig. 3.26 IT and CCT diagrams for 42CrMo4

environment. IT diagrams describe the crystal transformations due to isothermal holding, whereas CCT diagrams represent the continuous cooling processes at various rates. Both IT and CCT diagrams are determined experimentally. Grind-hardening process is described by CCT diagrams, since the cooling rate is high. In order to achieve the highest possible hardness, thus 100 % transformation of the crystal structure to martensite, the cooling curve should not enter the bainite area. The temperature where the Martensitic transformation begins (*Ts*), depends on the steel composition.

However, grind hardening and all other surface hardening processes are characterized by very high heating rates and brief austenitizing periods. These characteristics have a significant effect both on the metallurgy transformations and the temperature at which these are realized (Fig. 3.27).

3.6.2 Austenitization Temperature

The austenitizing temperature depends on the heating rate, the peak temperature and the holding time of a specific material. In the case of 100Cr6, the correlation of these parameters was experimentally determined by Liedtke and Jonsson [43]

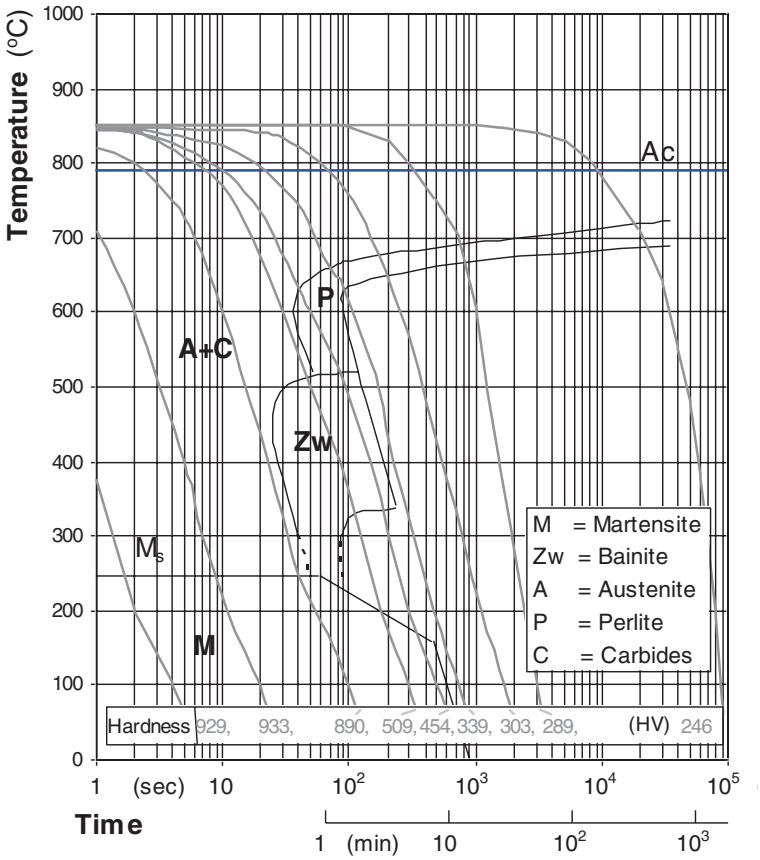

Fig. 3.27 CCT diagram for 100Cr6 steel for 860 °C austenitizing temperature

and is shown in Fig. 3.28. The heating rate achieved during grind hardening always exceeds 300 K/s [11, 12] and thus, based on Fig. 3.28, the austenitizing temperature is found to be 920 °C. Knowing the temperature field and the austenitizing temperature, we are led to the determination of the HPD.

3.6.3 Martensitization Temperature

The austenitization of the workpiece in elevated temperature, has another critical metallurgy effect that has to be taken into consideration as it reduces significantly the M_s temperature. In the case of 100Cr6, when the workpiece has been austenitized at 860 °C, the martensite transformation begins at 245 °C, but for an austenitization temperature of 1050 °C, the martensite transformation will not start until the temperature falls beneath 135 °C. Since in the grind-hardening process

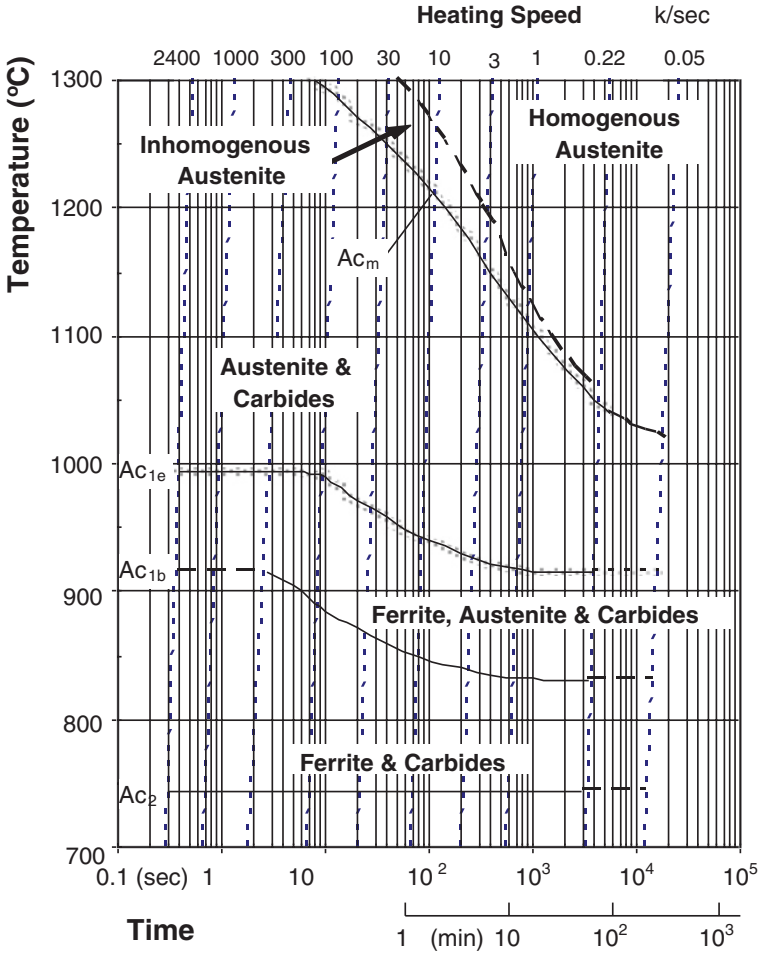

Fig. 3.28 Austenitization temperature as a function of heating rate for 100Cr6

the peak austenitizing temperature depends not only on the process parameters but also on the distance from the workpiece surface, the M_s line of the CCT diagram has to be determined for each point in the workpiece. For the determination of the relation between the M_s and the peak austenitizing temperatures, the experimental data stated in [44] were used and an exponential relation was assumed to relate these parameters (Fig. 3.29):

$$M_s = 2835.7e^{-0.0029T} \tag{3.60}$$

Based on the above considerations and using the temperature history calculated for each workpiece node with the FEA analysis, a modified CCT diagram, presenting different A_c and M_s temperatures, can be plotted for each node. Based

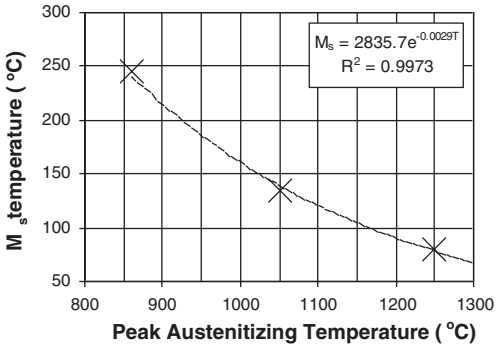

Fig. 3.29 M_s temperature dependence on peak austenitizing temperature for 100Cr6 (based on [44])

on these CCT diagrams, the microstructure and the micro-hardness HV_{CCT} on each workpiece node can be estimated. It should be noted however that the CCT diagram determined using this methodology, does not take into account the fact that during grind hardening, the workpiece undergoes high deformations at high strain rates which further alters the CCT diagram.

3.6.4 Retained Austenite

The micro-hardness calculated from the CCT diagram is based on the assumption that all austenite is transformed to martensite. However, the austenite transformation to martensite ends at a temperature, quite lower than that of the ambient. The extent of athermal transformation depends only on the degree of undercooling below the M_s temperature. The volume fraction of martensite transformation during undercooling, can be determined by using an experimental equation developed by Koistinen and Marburger [45] for Fe-C alloys containing between 0.37 and 1.1 % carbon:

$$f = 1 - e^{-1.10\times10^{-2}\Delta T} \tag{3.61}$$

where f is the volume fraction of martensite and ΔT is the undercooling below the M_s temperature.

3.6.5 Micro-Hardness

The hardness of the retained austenite is equal to that of the pre-treated material and therefore, the presence of retained austenite reduces the overall hardness of the workpiece. Considering that the overall hardness follows the inverse lever rule for a two-phase system, the overall hardness is given by the following equation:

$$HV = f \cdot HV_{\mathrm{CCT}} + (1 - f) \cdot HV_{\mathrm{Ret.Austenite}} \tag{3.62}$$

where HV is the overall hardness, HV_{CCT} is the hardness read from the CCT diagram for the specific cooling path and $HV_{Ret.Austenite}$ is the hardness of the retained austenite.

3.6.6 Hardness Penetration Depth

The hardness penetration depth (HPD) is a quantitative metric for characterizing the process outcome. It is also a design characteristic—specification of the component. From the process perspective, HPD is defined as the distance from the workpiece surface to its depth, where the hardness value is reduced to 80 % of the nominal value. There are a couple of different approaches in predicting the HPD theoretically. The HPD can be determined from the theoretically determined hardness profile as proposed by Salonitis and Chryssolouris [11] or can be approximated to be equal to the depth where the temperature exceeds that of austenitization as pointed out by Chryssolouris et al. [12]. It should be noted though, that the latter method can be used only when the critical quenching has been achieved, i.e. when bulky workpieces are hardened [12] and/or when coolant fluid is used for the grind hardening of small size workpieces [11]. The two methods were compared by Salonitis and Chryssolouris [11] and it was shown that the maximum error caused in the HPD estimation from the austenitization depth was ca. 8 %.

3.6.6.1 Maximum Achievable Hardness Penetration Depth

Both experimental and theoretical results indicate that HPD increases as the heat entering the workpiece material does. The heat entering the workpiece is a function of the process parameters. Increasing the depth of cut increases the material removal and thus the heat generation rates. On the other hand, the decrease in the workpiece speed allows for more heat to be dissipated within the workpiece material. However, higher values of heat entering the workpiece will result in a subsequent increase of the workpiece surface temperature. The workpiece temperature should not exceed the melting point of the material so as to avoid grain growth and increased retained austenite after quenching [42] that reduces the hardness of the treated layer [11]. Furthermore, the rapid melting and solidification that may occur in the heat affected zone during the surface hardening processes, results in coarsening and dissolution of the strengthening phases that degrade the strengthening of this area. The melting point depends on the workpiece material composition and can be calculated from its Fe-Fe_3C diagram [46]. In the case of 100Cr6, for example, this critical temperature is equal to 1315 °C. Therefore, the heat flux rate inducing the melting temperature at the workpiece surface is the maximum allowable rate to be generated during grind hardening for a specific set of depth of cut and workpiece speed. The HPD that will result from this heat flux rate will be the maximum to be achieved from this set of parameters.

3.6.7 Model Implementation and Validation

For the estimation of the metallurgical transformations, the hardness profile and the hardness penetration depth; the temperature field distribution and its evolution over time is required as input. The steps to be followed in order to fully characterize the process outcome are presented in Fig. 3.30, and can be considered as the continuation of Fig. 3.21.

3.6.7.1 CCT Diagram Modification

The available CCT diagrams are for conventional heat treatment processes where both heating and cooling takes place under controlled quasi-stationery rates. However, since in grind hardening both the heating and cooling rates are very rapid, the CCT diagram needs to be modified accordingly. Indicatively, the procedure for estimating the modified CCT diagram is presented hereafter. In Fig. 3.31, the temperature evolution for different depths below the workpiece surface is shown, as well as the various critical temperatures for the metallurgical changes.

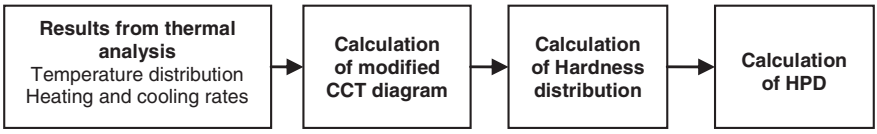

Fig. 3.30 Metallurgical changes modelling steps

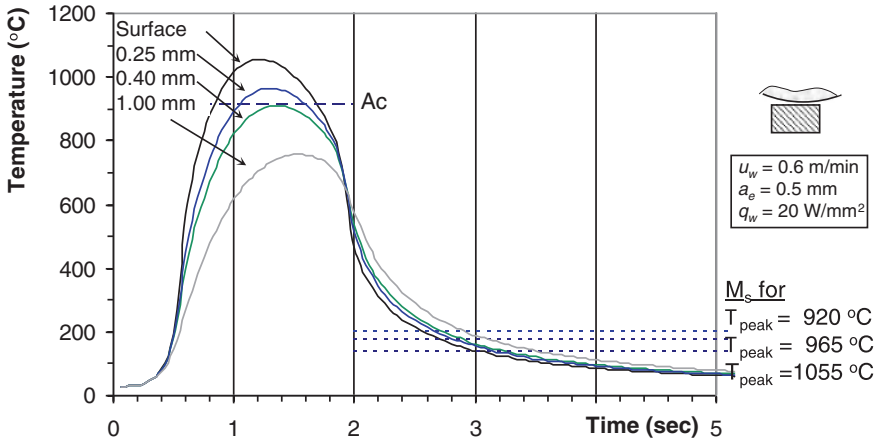

Fig. 3.31 Temperature distribution as a function of time and distance from the workpiece surface

The austenitization temperature in this case was estimated based on the method presented in Sect. 3.6.2, and is a function of the heating rate. For the process parameters presented in Fig. 3.31, the heating rate at the workpiece surface is close to 1,200 K/s, whereas in the depth where the temperature equals that of austenitization is about 700 K/s. Based on the data presented by Liedtke and Johnson [43] and Fig. 3.28, austenitzation temperature equals 920 °C for heating rates that exceed 300 K/s. On the other hand, the martzitization temperature can be calculated using Eq. (3.60), as a function of the peak temperature. Due to the fact that the peak temperature is different for every location on the workpiece, different martensitization temperatures are calculated (Fig. 3.31). Based on such calculations, the CCT diagram can be modified for every point in the workpiece. Indicatively, Fig. 3.32 presents the modified CCT diagram that was estimated for the temperature distribution shown in Fig. 3.31.

3.6.7.2 Hardness Distribution Estimation

The overall hardness will be different at each depth and can be calculated from the modified CCT diagram Eq. (3.62) as a function of the volumetric concentration of

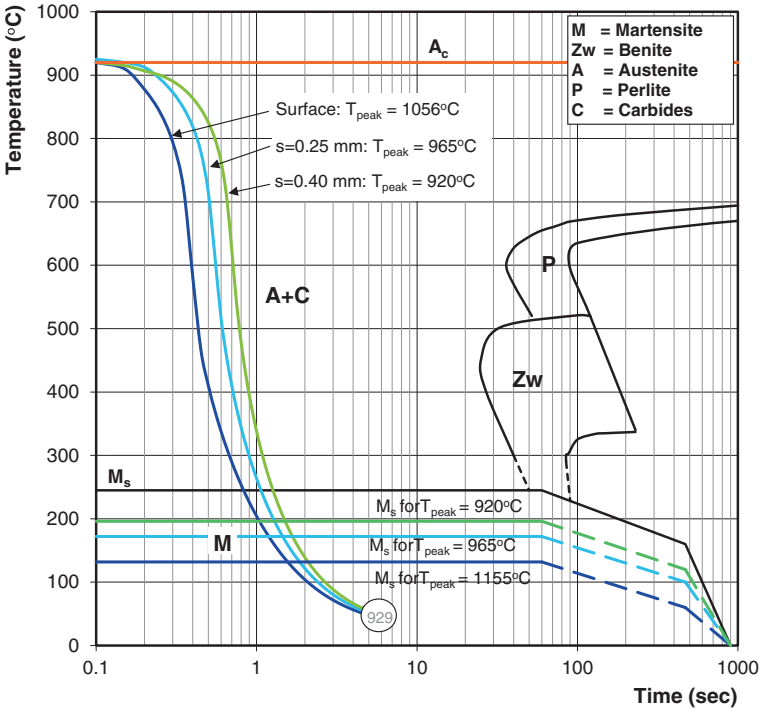

Fig. 3.32 Modified CCT diagram

Table 3.1 Hardness distribution calculation

	Distance from surface		
	0.00 mm	0.25 mm	0.40 mm
Heating rate (K/s)	1200	850	700
Austenitization temperature (°C)	920	920	920
Peak temperature (°C)	1056	965	920
Martensite temperature (Eq. 3.60 in °C)	133	173	197
Retained austenite (Eq. 3.61 in %)	41.3	36.5	35.5
CCT hardness (HV)	929	929	929
Calculated hardness (Eq. 3.62 HV)	**690**	**735**	**740**

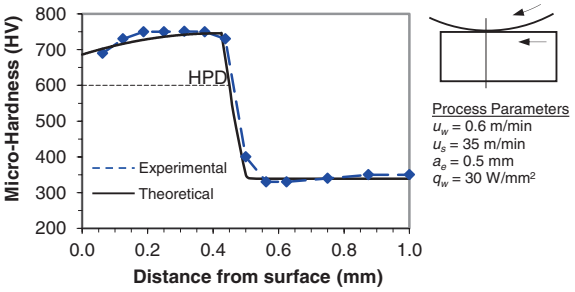

Fig. 3.33 Model verification for micro-hardness calculation

retained austenite. As it has been already noted, this is a function of the extent of undercooling below the martensitization temperature. As a result, the concentration of the retained austenite is maximum at the workpiece surface and decreases with the distance from the surface. Table 3.1 summarizes the calculated micro-hardness and Fig. 3.33 presents the experimental verification of the predictions.

3.6.7.3 Hardness Penetration Depth Estimation

It has been already stated that HPD is defined as the distance from the workpiece surface to its depth, where the hardness value is reduced to 80 % of the nominal value. Based on the calculated hardness distribution (Fig. 3.33), the HPD can be determined. Alternatively, it can be estimated from the depth where the temperature exceeds the austenitization temperature, as pointed out by Chryssolouris et al. [12]. They compared the two methods with experimental measurements and concluded that the calculation of the HPD using the hardness distribution provides better agreement with the experimental results. However, the effort needed for the determination of the hardness distribution is quite copious.

3.7 Modelling of Residual Stresses

The residual stresses are the result of inhomogeneous plastic deformations during quenching. The generation of the residual stresses is quite complex, with numerous affecting factors. The material type is one of the most important ones with heat transfer coefficient, thermophysical and mechanical properties, and phase composition influencing greatly the residual stresses. The higher the yield strength of the material the more elastic the thermal and transformation-induced macroscopic stresses will be generated in the part to be quenched. Thus, the residual stresses in general will be lowered with increasing yield strength of the material.

A typical residual stress profile generated is presented in Fig. 3.34. The most important factors are presented, being (a) the surface residual stress magnitude, (b) the maximum value measured and (c) the distance from the processed surface where the maximum value occurs and, finally (d) the beneficial depth.

Thermal surface treatments always result in residual stresses. The reasons for these stresses have been identified in a number of studies and can be summarized into (i) the thermal stresses due to thermal expansion or contraction during heating and cooling of the workpiece and (ii) the density changes due to the phase transformations in the workpiece material. In case of multiphase materials, residual stresses are also generated due to the different thermal expansion coefficients of the various phases and due to chemical reaction products formed on the surface of the workpiece material.

In general when heat treating workpieces, the cooling rate at the surface is higher than at the centre. The early thermal contraction at the surface is resisted by the incompressible core, resulting in tensile yielding at the surface. The continuous temperature reduction results in contraction of the workpieces core pulling the surface inwards. As a result of this inward pulling, compression stresses are generated near the surface. In materials with phase transformation, anisotropic volume change due to martensitic transformation adds to the complexity and magnitude

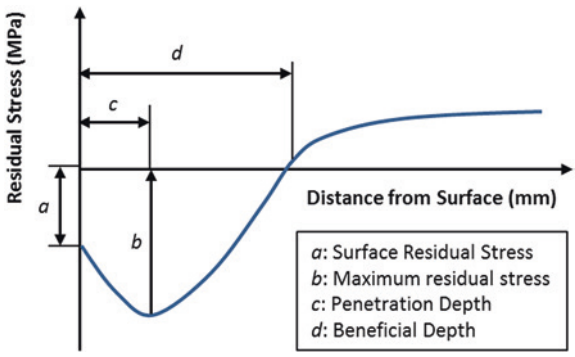

Fig. 3.34 Typical surface residual stress profile [47]

of the residual stress pattern. The residual stress system is self-equilibrating; if certain regions have compressive residual stresses, then somewhere else there must be offsetting tensile stresses.

For the case of grinding, surface residual stresses is a result of the thermal deformation due to heat dissipation in the grinding zone, the pressure between the grinding wheel and the workpiece, and the phase transformation of the material structure [48]. The balance between these three different mechanisms defines whether the final residual stresses are compressive or residual. It has been shown in past studies, focusing though on grinding and not grind hardening, that the pressure applied from the grinding wheel to the workpiece induces compressive residual stresses. On the other hand thermal deformation due to the heat dissipation results in tensile residual stresses [49]. The challenge is to incorporate the resulting residual stresses due to phase transformation. Phase change results in volume change; depending on whether the new structure occupies more space than the original phase the residual stresses can be either compressive or tensile. For the case of grind hardening we observe two subsequent phase transformations. From ferrite/perlite mixture before grinding to austenite (existing only when the workpiece material is above eutoctoid temperature) during the processing and finally to martensite due to quenching. Martensite presents body-centred tetragonal (BCT) crystal structure whereas ferrite presents body-centred cubic (BCC) crystal structure [42]. Since BCT occupies more space than BCC, martensitic phase transformation results into compressive residual stresses.

3.7.1 Modelling Using Finite Element Analysis

Similarly, for the case of residual stresses modelling, the thermal model developed is used as a basis. Thermal elements are replaced with elastic-plastic elements. The resulting model undergoes a non-linear elastic-plastic structural analysis using temperature-dependent material properties and a multi-linear isotropic hardening model. The non-linear mechanical analysis problem is described by the following general finite element equation:

$$[K(T)]\{u(t)\} + \{F(t)\} + \{F_{\text{th}}(t)\} = 0 \tag{3.63}$$

where $[K(T)]$ is the temperature-dependent stiffness matrix, $\{F(t)\}$ is the external load vector, $\{F_{\text{th}}(t)\}$ is the temperature load vector and $\{u(T)\}$ is the displacement vector.

For each load step, the nodal temperatures from the thermal analysis are read into the structural analysis. Nodal temperatures from thermal results are continued to be read into the structural analysis until the time when the model temperature has reached the environmental one. The structural boundary conditions set to workpiece are quite simple; all nodes at the bottom end of the workpiece are fixed to all directions. The structural loading includes the application of pressure

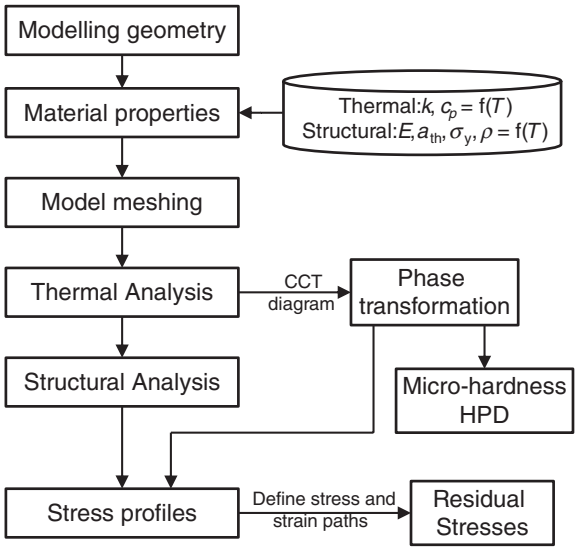

Fig. 3.35 Modelling approach for calculating residual stresses [50]

resulting from the grinding wheel–workpiece interaction at the elements that corresponds to the contact length for each load step. The non-linearity of material properties is taken into account through the von-Mises criterion, and plasticity is taken into consideration through kinematic strain-hardening law. The non-linear equation system solution is achieved through the Newton–Raphson algorithm, whereas Newmark integration scheme is applied for the numerical integration in the time domain. Salonitis [50] presented graphically the approach for predicting the residual stresses using FEA as shown in Fig. 3.35.

3.7.2 Model Implementation and Validation

Salonitis [50] validated this model for the case of grind hardening of AISI 1050 workpiece material both under wet and dry conditions. His analysis indicated that grind hardening without the application of coolant fluid result in tensile residual stresses across the whole depth of the heat treated layer (Fig. 3.36). The FEA model indicated that during dry grind hardening, the driving mechanism for the resulting residual stresses is the thermal deformation due to the high heat source generated in the grinding arc. Additionally, higher workpiece material results in lower martensite onset temperatures that leads to higher concentration of retained austenite. Austenite presents face-centred cubic (FCC) lattice structure with quite similar volume with original ferrite (BCC), thus the compressive stresses due to phase transformation are limited.

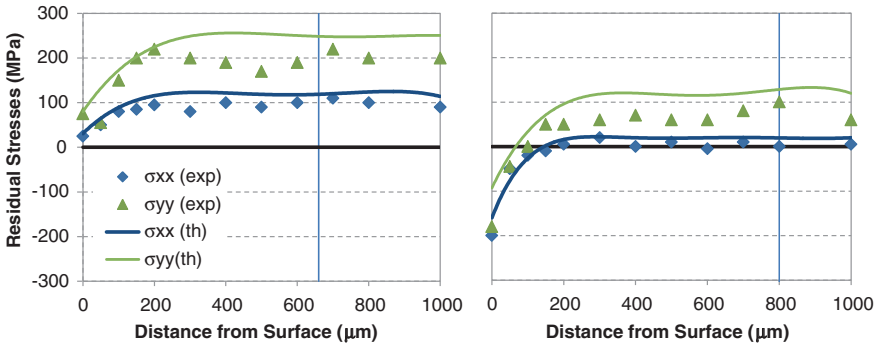

Fig. 3.36 Residual stresses after (*left*) dry and (*right*) wet grind hardening at the middle of the workpiece (*Vertical line* indicates the length of hardened layer) [50]

3.8 Integration of Models

Six models have been presented in the previous sections for simulating various aspects of the grind-hardening process. The models can be integrated all together for the holistic modelling of the grind-hardening process. In that case, we can identify five major phases that are sequentially connected for the estimation of the hardness profile, hardness penetration depth and residual stresses as a function of process parameters and the specification of the grind-hardening wheel (as can be seen in Fig. 3.37). During the first phase (phase A), the grinding forces as a function of process parameters and grinding wheel specification are determined. During the second phase (phase B), the heat generated within the grinding zone and its partition to the various heat sinks is estimated. In the subsequent phase (phase C), the temperature distribution along with the heating and cooling rates are estimated using finite element analysis. Phase D deals with the determination of the heat penetration depth and the micro-hardness distribution based on the estimated modified CCT diagrams. Finally, within the last phase (E) the residual stresses are estimated by solving the coupled thermal and structural finite element model.

Such an analysis can be used for developing process "maps" (a database) for the prediction of the process outcome as a function of process parameters. This database is based on diagrams linking, as an example, the hardness penetration depth with the heat flux entering the workpiece for a number of combinations of process parameters. Figure 3.38 presents an abstract of such a database developed by Salonitis [51] for the prediction of hardness penetration depth. Additionally, in Fig. 3.39, the database maximum hardness penetration depth diagram is presented.

3.8.1 Integrated Model and Database Validation

Salonitis et al. [52] used the database for estimating the process parameters to be used for achieving a specific hardness distribution and hardness penetration depth

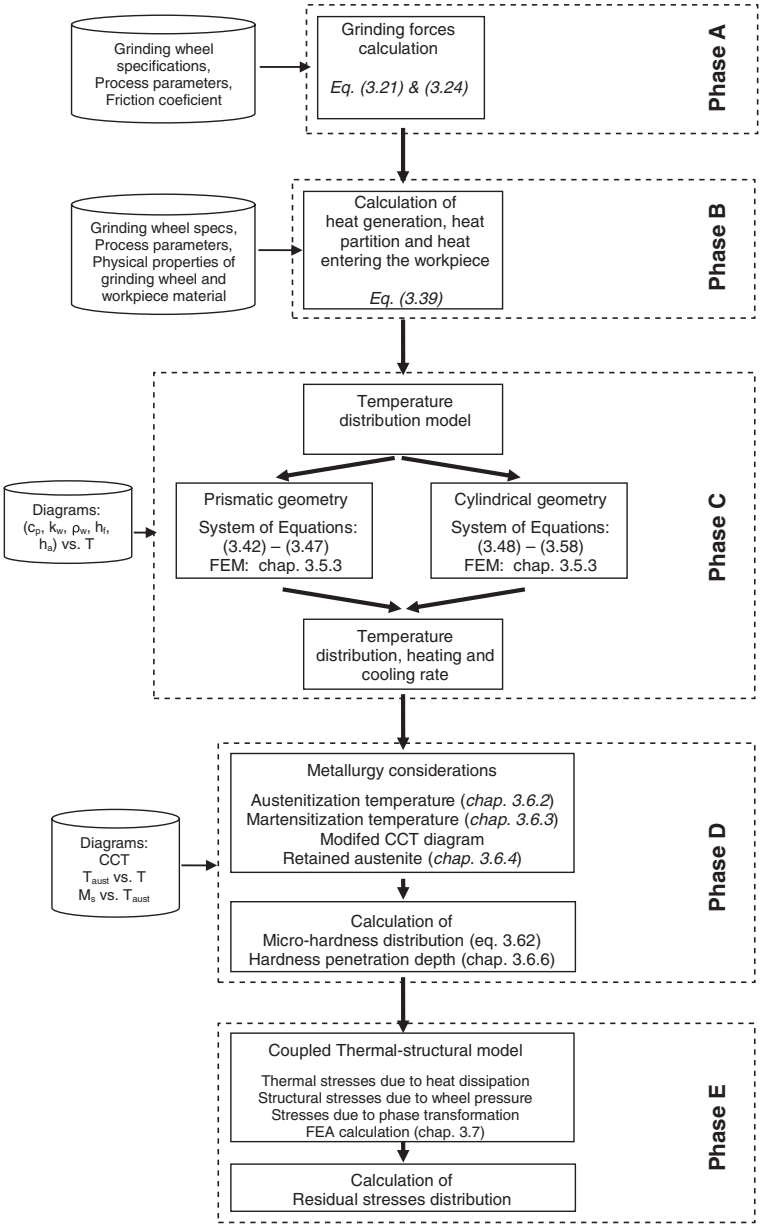

Fig. 3.37 Holistic model for grind-hardening simulation

to an actual industrial component (V-shaped guide). Having as a starting point the requirements and limitations, i.e. knowing the requested HPD and having a limitation on a specific process parameter (e.g. the feed speed), the heat flux can be determined for this set of variables, from the database of charts shown in Fig. 3.38.

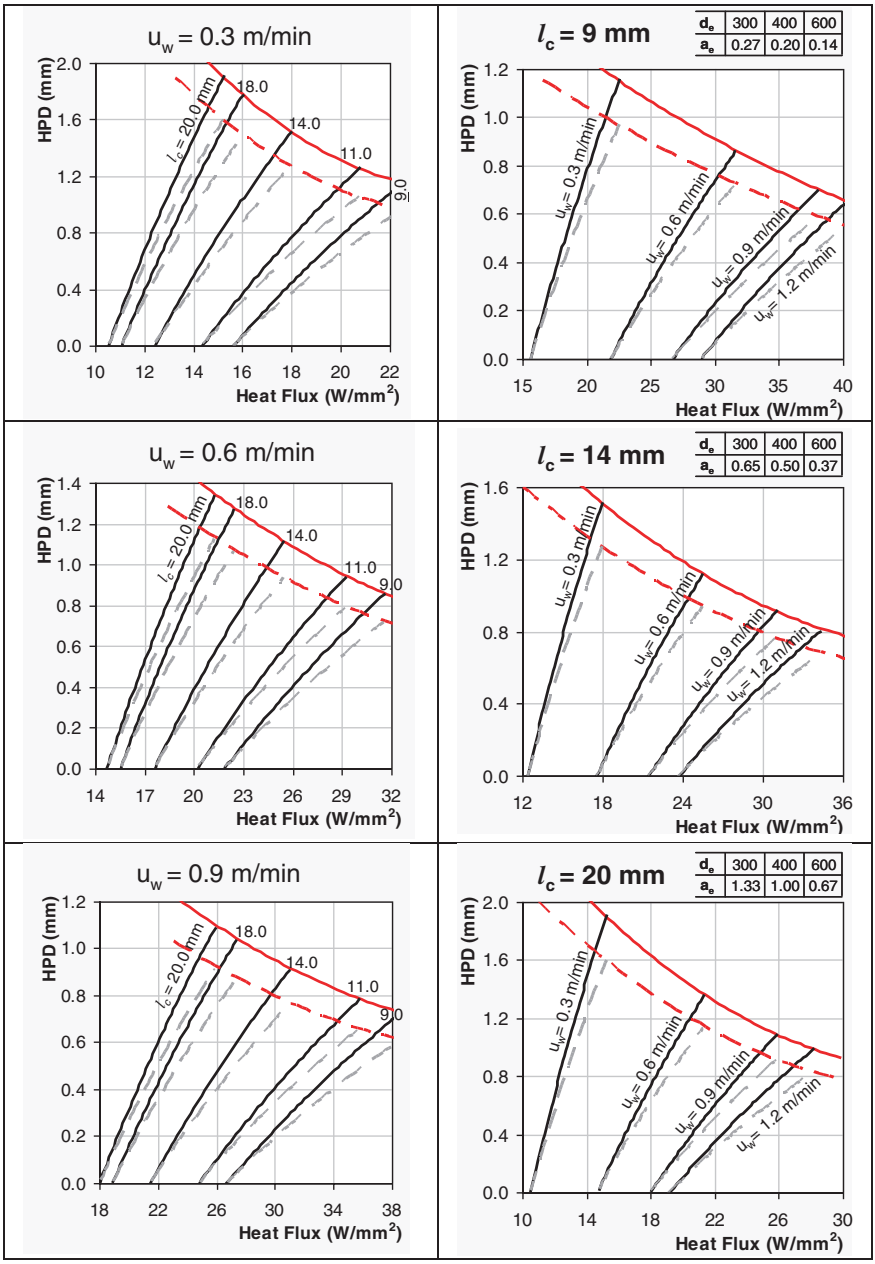

Fig. 3.38 Database diagrams for predicting the HPD as a function of process parameters (for AISI 52100—*dashed lines* are the experimentally tuned predictions) [51]

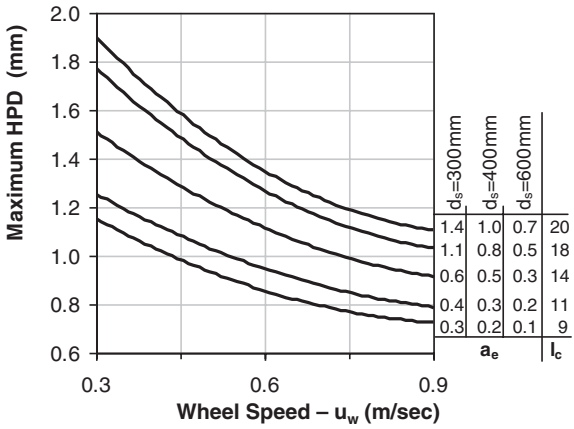

Fig. 3.39 Maximum hardness penetration depth predictions [51]

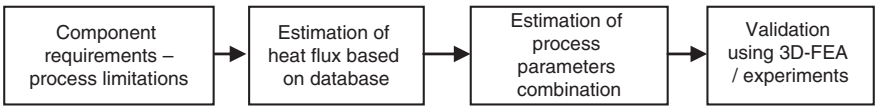

Fig. 3.40 Methodology for estimating the process parameters based on the product requirements and the process limitations

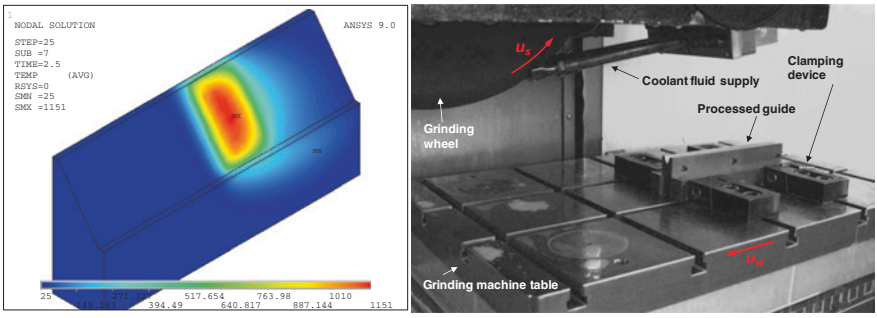

Fig. 3.41 *Left* Temperature field for $u_w = 0.6$ m/min, *Right* Experimental setup

In most cases, more than one combination of process parameters will give the requested result; the final selection lies in other issues, some of which are: the availability in grinding wheels, the grinding wheel wear, the grinding machine capabilities and the requested productivity. Figure 3.40 presents such an approach for estimating the process parameters graphically.

The V-shaped guide had to be hardened on the surface of both flanks, with a minimum surface hardness of 650 HV1 and a hardening depth of at least 0.3 mm. Using the database in Fig. 3.38, the requested HPD can be achieved with various combinations of process parameters. Some of the combinations can be rejected even before validation based on experience. For validation of the predictions, both a 3-D FEA model and experimental measurements were developed and used (Fig. 3.41).

References

1. Toenshoff HK, Peters J, Inasaki I, Paul T (1992) Modelling and simulation of grinding processes. CIRP Ann Manuf Technol 41(2):677–688
2. Salonitis K, Stavropoulos P, Kolios A (2014) External Grind Hardening Forces Modelling and Experimentation. Int J Adv Manuf Technol 70(1–4):523–530
3. Malkin S (1989) Grinding technology: theory and applications of machining with abrasives. Ellis Horwood, Chichester
4. Malkin S, Cook NH (1971) The wear of grinding wheels. Part 1. Attritious wear. ASME J Eng Ind 93:1120–1128
5. Hou ZB, Komanduri R (2003) On the mechanics of the grinding process—Part I. Stochastic nature of the grinding process. Int J Mach Tools Manuf 43:1579–1593
6. Kannapan S, Malkin S (1972) Effects of grain size and operating parameters on the mechanics of grinding. ASME J Eng Ind 94:833
7. Lichun L, Jizai F, Peklenik J (1980) A study of grinding force mathematical model. CIRP Ann Manuf Technol 29(1):245–249
8. Mishra VK, Salonitis K (2013) Empirical estimation of grinding specific forces and energy based on a modified werner grinding model. Procedia CIRP 8:287–292
9. Lavine AS (1991) Thermal aspects of grinding: the effect of heat generation at the shear planes. CIRP Ann Manuf Technol 40(1):343–345
10. Lavine AS (2000) An exact solution for surface temperature in down grinding. Int J Heat Mass Transf 43:4447–4456
11. Salonitis K, Chryssolouris G (2006) Cooling in grind hardening operations. Int J Adv Manuf Technol 33:285–297
12. Chryssolouris G, Tsirbas K, Salonitis K (2005) An analytical, numerical and experimental approach to grind hardening. SME J Manuf Process 7(1):1–9
13. Rowe WB, Morgan MN, Allanson DA (1991) An advance in the modelling of thermal effects in the grinding process. CIRP Ann Manuf Technol 40(1):339–342
14. Rowe WB, Morgan MN (1993) The effect of deformation on the contact area in grinding. CIRP Ann Manuf Technol 42(1):409–412
15. Zhou ZX, Van Lutterwelt CA (1992) The real contact length between grinding wheel and workpiece—a new concept and a new measuring method. CIRP Ann Manuf Technol 41(1):387–391
16. Lavine AS, Malkin S, Jen TC (1989) Thermal aspects of grinding with CBN wheels. CIRP Ann Manuf Technol 38(1):557–560
17. Rowe WB, Black SCE, Mills B, Qi HS, Morgan MN (1995) Experimental investigation of heat transfer in grinding. CIRP Ann Manuf Technol 44(1):329–332
18. Rowe WB, Morgan MN, Black SCE, Mills B (1996) A simplified approach to control of thermal damage in grinding. CIRP Ann Manuf Technol 45(1):299–302
19. Rowe WB, Black SCE, Mills B (1996) Temperature control in CBN grinding. Int J Adv Manuf Technol 12:387–392

20. Rowe WB, Morgan MN, Black SCE (1998) Validation of thermal properties in grinding. CIRP Ann Manuf Technol 47(1):275–279
21. Guo C, Malkin S (1992) Heat transfer in grinding. J Mater Process Manuf Sci 1:16–27
22. Guo C, Malkin S (1994) Analytical and experimental investigation of burnout in creep-feed grinding. CIRP Ann Manuf Technol 43(1):283–286
23. Guo C, Malkin S (1996) Effectiveness of cooling in grinding. Trans North Am Manuf Res Inst SME 1996 (NAMRI/SME) XXIV:111–116
24. Guo C, Malkin S (2000) Energy partition and cooling during grinding. SME J Manuf Process 2(3):151–157
25. Jin T, Cai GQ, Jeong HD, Kim NK (2001) Study on heat transfer in super-high-speed-grinding: energy partition to the workpiece in HEDG. J Mater Process Technol 111:261–264
26. Toenshoff HK, Brinksmeier E, Choi H-Z (1987) Abrasives and their influence on forces, temperatures, and surface. In: Proceedings of the 15th North American manufacturing research conference, pp 70–89
27. Rowe WB, Pettit JA, Boyle A, Moruzzi JL (1988) Avoidance of thermal damage in grinding and prediction of the damage threshold. CIRP Ann Manuf Technol 37(1):327–330
28. Salonitis K, Chryssolouris G (2007) Thermal analysis of grind-hardening process. Int J Manuf Technol Manage 12(1/2/3):72–92
29. Salonitis K, Chondros T, Chryssolouris G (2008) Grinding wheel effect in the grind-hardening process. Int J Adv Manuf Technol 38(1–2):48–58
30. Rowe WB (2001) Thermal analysis of high efficiency deep grinding. Int J Mach Tools Manuf 41:1–19
31. Rowe WB, Jin T (2001) Temperatures in high efficiency deep grinding (HEDG). CIRP Ann Manuf Technol 50(1):205–208
32. Hahn RS (1962) On the nature of the grinding process. In: Proceedings of the 3rd machine tool design and research conference, pp 129–154
33. Kim NK, Guo C, Malkin S (1997) Heat flux distribution and energy partition in creep-feed grinding. CIRP Ann Manuf Technol 46(1):227–232
34. Jin T, Stephenson DJ (2003) Investigation of the heat partitioning in high efficiency deep grinding. Int J Mach Tools Manuf 43:1129–1134
35. Chang CC, Szeri AZ (1998) A thermal analysis of grinding. Wear 216:77–86
36. Chiu N, Malkin S (1993) Computer simulation for cylindrical plunge grinding. CIRP Ann Manuf Technol 42(1):383–387
37. Eda H, Ohmura E, Yamauchi S (1993) Computer visual simulation on structural changes of steel in grinding process and experimental verification. CIRP Ann Manuf Technol 42(1):389–392
38. Lavine AS (1988) A simple model for convective cooling during the grinding process. J Eng Ind 110:1–6
39. Snoeys R, Maris M, Peters J (1978) Thermally induced damage in grinding. CIRP Ann Manuf Technol 27:571–579
40. Carslaw HS, Jaeger JC (1959) Conduction of heat in solids. Oxford University Press, London
41. Jin T, Cai GQ (2001) Analytical thermal models of oblique moving heat source for deep grinding and cutting. J Manuf Sci Eng 123:185–190
42. Krauss G (1993) Steels: heat treatment and processing principles, ASM International, Materials Park
43. Liedtke D, Jonsson R (1996) Warmebehandlung. Expert Verlag
44. Liedtke D, Jonsson R (1954) Atlas zur Waermebehandlung der Stahle, 1st edn. Verlag stahleisen mbH, Duesseldorf
45. Koistinen DP, Marburger RE (1959) A general equation prescribing the extent of the Austenite-Martensite transformation in Pure Iron-Carbon alloys and plain Carbon steels. Acta Metall 7:59–60
46. Pollack H (1988) Materials science and metallurgy, 4th edn. Prentice-Hall, Englewood Cliffs

47. Umbrello D, Ambrogio G, Filice L, Shivpuri G (2008) A hybrid finite element method–artificial neural network approach for predicting residual stresses and the optimal cutting conditions during hard turning of AISI 52100 bearing steel. Mater Des 29:873–883
48. Mahdi M, Zhang L (1999) Applied mechanics in grinding. Part 7: residual stresses induced by the full coupling of mechanical deformation, thermal deformation and phase transformation. Int J Mach Tools Manuf 39:1285–1298
49. Mahdi M, Zhang LC (1997) Applied mechanics in grinding-V. Thermal residual stresses. Int J Mach Tools Manuf 37:619–633
50. Salonitis K (2014) On surface grind hardening induced residual stresses. Procedia CIRP 13:264–269
51. Salonitis K (2006) A methodology for the prediction of the hardness distribution and the hardness penetration depth caused by grind-hardening process. Ph.D. dissertation, University of Patras, Patras, Greece
52. Salonitis K, Stavropoulos P, Stournaras A, Chryssolouris G (2007) Finite element modeling of grind hardening process. In: Proceedings of 10th CIRP International Workshop on Modeling of Machining Operations, pp 117–123